Honours Year Thesis (Academic Year 2004/05)

Experiments with Multi-Photon States

In partial fulfilment for a Degree in Bachelor of Science (Hons.) in Physics

Poh Hou Shun

Supervisors:
Assistant Professor Antia Lamas-Linares
Associate Professor Christian Kurtsiefer

Department of Physics, Faculty of Science
National University of Singapore
10 Kent Ridge Road, Singapore 117546

ACKNOWLEDGEMENTS

I would like take my chance here to firstly thank my supervisors, Prof. Antia and Prof. Christian for their unending support in this experiment. Their humourous take on things and willingness to help any students in doubt have made me even more interested and devoted to this project. Of course, this experiment was no solo affair, it required a lot of external help and guidance and in the QIT group there was no shortage of either. I would like to thank Meng Khoon, our resident guru on all things. His simple comments make the difference between days of hunting for an unknown problem or a quick and ingenious fix. I am also grateful to Alex and Ivan. Their expertises on the down-conversion setup have made the process of alignment almost enjoyable. Lastly I would like to extend my heartfelt gratitude to Chune Yang, the graduate student whom I have worked with for the past year on this project. Without his help, this project will not be able to finish on time.

CONTENTS

ABSTRACT

Most experiments with entangled photons up until today involved the use of entangled pairs that were generated in first order parametric down-conversion. It is only recently that pulsed laser systems are used to gain access to the higher order terms in the down-conversion process. This experiment aims mainly to look into the various intricacies involved in setting up a source of 4-photon states that are generated through a pulsed type-II parametric down-conversion process. With the source, an experimental violation of the spin-$\frac{1}{2}$ and spin-1 Bell's inequality can then be implemented to test the quality of entanglement. Various other experiments involving 4-photon states can also be carried out with the use of this source.

Chapter 1
INTRODUCTION

1.1 HISTORICAL OVERVIEWS

This field of research can be said to have started with a paper published in 1935 by Einstein, Podolsky and Rosen [11] questioning the completeness of the quantum mechanical description of reality. The paper considered a two-particle system prepared in a state such that their relative position $x_1 - x_2$ and total momentum $p_1 + p_2$ have definite values. This is shown in Figure 1 [4]. Therefore when the position or momentum of one particle is measured, one can assign a definite value to the position and momentum of both particles. As the two measurements on the particles are independent of each other, the measurements must be elements of reality. Since there is no quantum mechanical equivalent, no operators which have eigenvectors that could describe the sharp values for these both elements of reality, they were lead to the conclusion that the quantum mechanical description is incomplete. It is then nature to hypothesize that the correlation observed are due to some, which up to this point, hidden variables which are proposed in various hidden-variable theories [6].

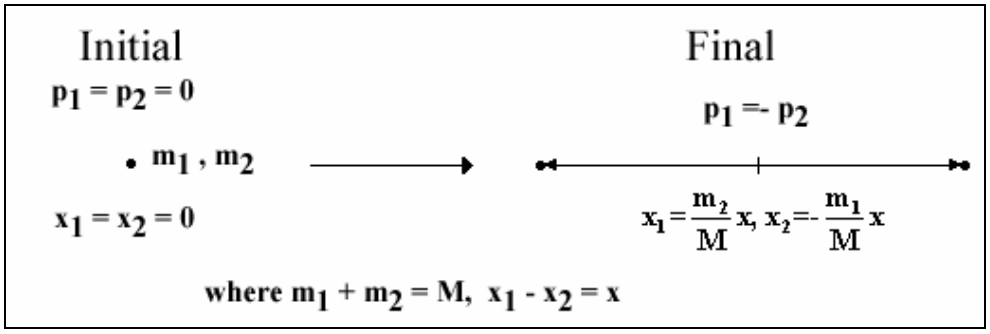

Figure 1 – EPR though experiment

This question regarding the presence of a hidden-variable theory remained unresolved until 30 years later when J.S. Bell came up with the Bell's inequality [6] which allows the quantum mechanical and local hidden-variable theory predictions to be distinguished. The original form of the Bell's inequality is shown below.

$$1+P\left(\vec{b},\vec{c}\right)\geq\left|P\left(\vec{a},\vec{b}\right)-P\left(\vec{a},\vec{c}\right)\right|$$

It is derived based on a more realistic experiment proposed by Bohm. This is shown in Figure 2. The system consists of two spin-$\frac{1}{2}$ particle prepared in a state such that the total spin is zero. $P\left(\vec{a},\vec{b}\right)$ is just the average value of the product of the spins and so on. The singlet spin state vector is given by

$$\left|\varphi\right\rangle=\frac{\left(\left|+,-\right\rangle-\left|-,+\right\rangle\right)}{\sqrt{2}}$$

where + and – corresponding to spin up and down respectively.

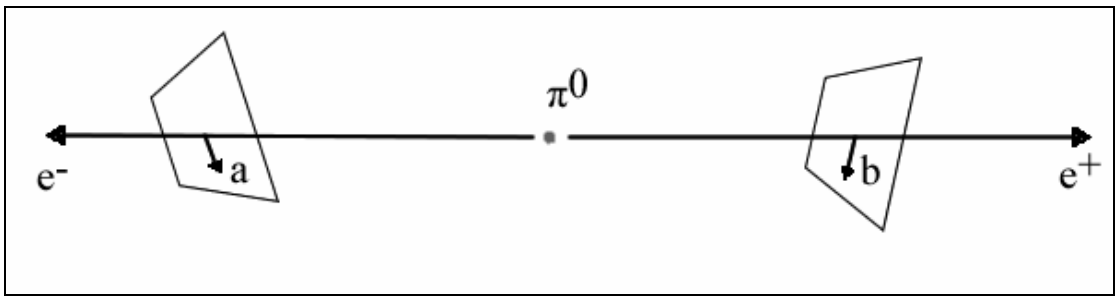

Figure 2 – EPR-Bohm experiment

As the total spin is zero, one can predict with certainty the spin of one atom in one axis after having measured the spin of the other in a parallel axis. It is the quantum mechanical prediction of this probability of correlation between two different arbitrary measurement axes that results in the violation of the Bell's inequality. From that point on, there have been many realizations of the Bohm-type experiment using sources that emits pairs of suitably correlated photons or spin-$\frac{1}{2}$ particles in a singlet state.

1.2 OPTICAL BELL TESTS

One of the first experiments with a source that emitted pairs of suitably correlated photons was the Aspect experiments [1-3]. The polarisation correlated photons were emitted in a radiative atomic cascade of calcium. However this has been replaced by the more efficient and simpler non-linear process of parametric down-conversion in modern experiments. While there have also been dramatic improvements in the optical elements and detection electronics, the basic principle behind the experiment remained the same.

1.2.1 THE ASPECT EXPERIMENTS

The Aspect experiments were a series of experiments ran by Alain Aspect and others in the early 1980s aimed at optically violating the Bell's inequality. The first experiment setup is shown in Figure 3 [2].

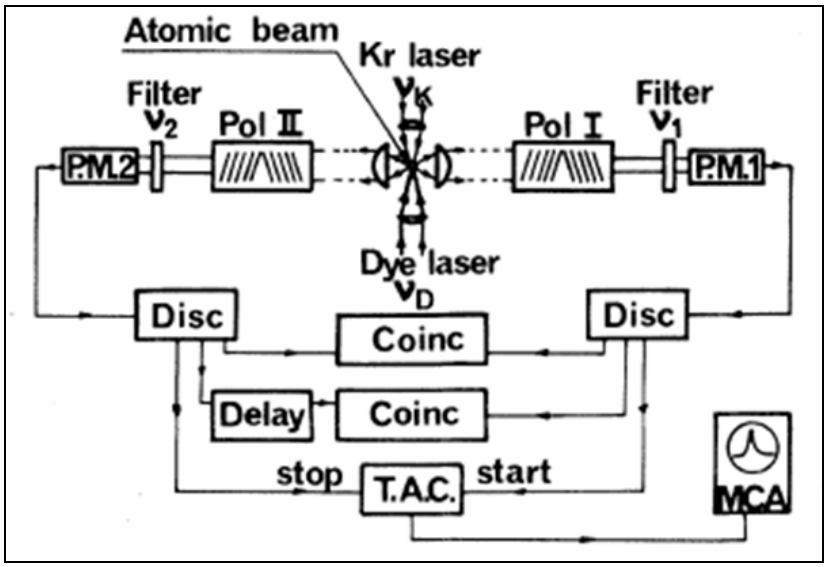

Figure 3 – The first Aspect experiment

The source generated photons which were correlated in polarisation by the process of radiative atomic cascade of calcium. These are then analysed by polariser consisting of glass plates stacked at Brewster angle. The detection circuit consisted of photomultiplier tubes, time-to-amplitude converter and a coincidence circuit. With this setup, they were able to observe violation of the spin-$\frac{1}{2}$ Bell's inequality by up to 9 standard deviations. Subsequent experiments involved the introduction space-like separations between the source and the detectors so as to eliminate the possibly of any communication between them in the time taken for the photons to travel the separation. Modifications were also done with time-varying analysers.

1.2.2 MODERN 2-PHOTON EXPERIMENT

In modern optical Bell tests, one of the main differences was that the source has been replaced with a more efficient process. The generation of the polarisation correlated

photons now relied on the non-linear optical process of parametric down-conversion. A typical setup is shown in Figure 4 [15].

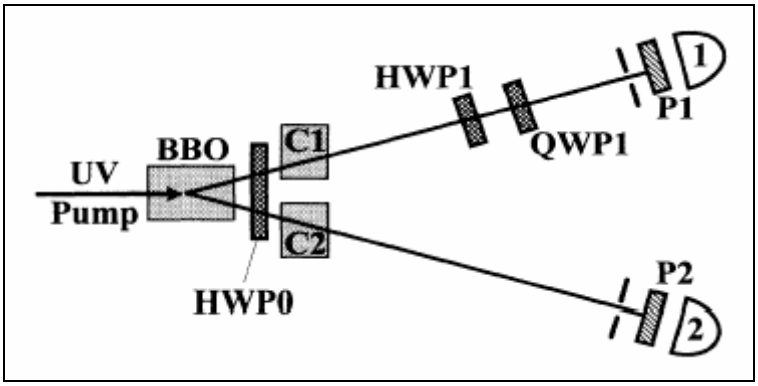

Figure 4 – A modern 2-photon experiment

From Figure 4, it can be seen that the down-conversion setup is now much simpler. Advances in birefringent materials have resulted in the development of efficient wave plates which were used both to the change the input state and to analyse them. Photomultiplier tubes have been replaced with silicon avalanche diodes detectors as they are more compatible with the wavelengths used. All these improvements have resulted in the violation of the spin-$\frac{1}{2}$ Bell's inequality by as much as 102 standard deviations with integration times as little as 5 minutes.

1.2.3 MODERN 4-PHOTON EXPERIMENT

The experiments mentioned so far all involved sources that generated entangled photon pairs. However the recent use of pulsed laser systems has made it possible to generate 4-photon states in a second order parametric down-conversion process. Instead of a single photon being detected in each arm, two were detected. The first

setup of this kind that shows violation of a spin-1 Bell's inequality is shown in Figure 5 [13].

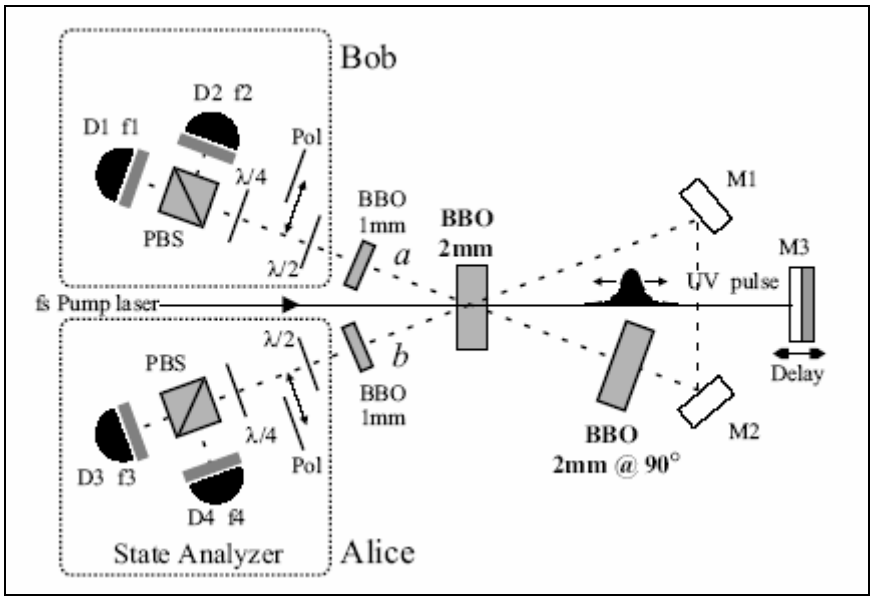

Figure 5 – A Modern 4-photon experiment

The down-conversion setup is similar to that of the 2-photon experiment with the exception that it used a 2-pass scheme in an attempt to increase the down-conversion efficiency. The analysers now have two output ports each for the detection of the four possible output state. Such a setup has shown a violation of the spin-1 Bell inequality by more than 13 standard deviations.

This is precisely what this experiment aims to accomplish. To implement a 4-photon source with a simpler 1-pass scheme that can be used for various other quantum information experiments.

Chapter 2
BELL'S INEQUALITY

The original Bell's theorem or Bell's inequality was formulated by John Bell in 1964 [6] in an attempt to answer the question raised by Einstein, Podolsky and Rosen [11] about the completeness of the quantum mechanical description of reality. In 1969, Clasuer, Horne, Shimony and Holt came up with the CHSH inequality [8] which is commonly used today. Like Bell's theorem, it was intended to distinguish between the predictions made by quantum mechanics and various local hidden-variable theories. Though currently there are many different inequalities, e.g. CH74 [7] that serve the same purpose, they are still collectively known as Bell's inequalities.

This chapter will detail the derivation of the CHSH inequality and its' maximum violation in 2 and 4-particle systems as predicted by quantum mechanics. It will also look into the experimental applications and the possible loopholes associated with these experiments.

2.1 DERIVATION OF BELL'S INEQUALITY (CHSH)

The derivation of the CHSH inequality [6] like any other Bell's inequalities starts with two fundamental assumptions. They are:

1. The correlations between Alice and Bob's measurement can be accounted for by a local realistic theory; also known as local hidden-variable theory. Simply put the correlations can be explained by some unknown variable that are set up at the source or anywhere else. This is also referred to as the 'realism condition'.

2. Alice's measurement outcome is independent of Bob's measurement settings, vice versa. This is also referred to as the 'locality condition'.

From the above assumptions, the joint probability of Alice and Bob's measurement, probability of Alice and Bob obtaining A and B as measurement outcome respectively, can be written in the following form:

$$P(A,B\,|\,\alpha,\ \beta,\ \lambda)\ =\ P(A\,|\,\alpha,\ \lambda)P(B\,|\,\beta,\ \lambda)$$

where α and β are any analyser settings at the Alice and Bob's side respectively. λ accounts for all local hidden-variables. Due to the 'locality condition', Alice and Bob's measurement are independent and thus the joint probability can be decoupled and be expressed as a product of the individual measurement probability.

In addition a correlation function can be written as the following

$$E^{HV}(\alpha,\beta) = \int \overline{A}(\alpha,\lambda)\overline{B}(\beta,\lambda)\, f(\lambda) d\lambda$$

where $\overline{A}$ and $\overline{B}$ are the average of the measurement outcome obtained by Alice and Bob with analyser setting α and β respectively. $f(\lambda)$ is a probability density function that is dependent on the hidden-variable λ.

In a dichotomic system, the measurement outcomes can be labelled as +1 or -1. Thus it must be true that the average of the measurement outcomes can be expressed as

$$\left|\overline{A}(\alpha,\lambda)\right| \le 1,\ \left|\overline{B}(\beta,\lambda)\right| \le 1$$

Consider the following

$$E^{HV}(\alpha,\ \beta) - E^{HV}(\alpha,\ \beta') = \int d\lambda\, f(\lambda)\overline{A}(\alpha,\lambda)(\overline{B}(\beta,\lambda) - \overline{B}(\beta',\lambda))$$

Since $\left|\overline{A}(\alpha,\lambda)\right| \le 1$, the above can be written as

$$\left|E^{HV}(\alpha,\ \beta) - E^{HV}(\alpha,\ \beta')\right| \le \int d\lambda\, f(\lambda)\left|\overline{B}(\beta,\lambda) - \overline{B}(\beta',\lambda)\right|$$

Similarly,

$$\left|E^{HV}(\alpha',\ \beta) + E^{HV}(\alpha',\ \beta')\right| \le \int d\lambda\, f(\lambda)\left|\overline{B}(\beta,\lambda) + \overline{B}(\beta',\lambda)\right|$$

In addition, since $\left|\overline{B}(\alpha,\lambda)\right| \le 1$, the above can be written as

$$\left|\overline{B}(\beta,\lambda) - \overline{B}(\beta',\lambda) + \overline{B}(\beta,\lambda) + \overline{B}(\beta',\lambda)\right| \leq 2$$

This then implies

$$S = \left|E(\alpha,\ \beta)\ -\ E(\alpha,\ \beta')\ +\ E(\alpha',\ \beta)\ +\ E(\alpha',\ \beta')\right| \leq 2$$

Thus with any hidden-variable theory, the value S can only be less than or equal to 2.

2.2 DERIVATION OF MAXIMUM VIOLATION OF BELL'S INEQUALITY

The quantum mechanical prediction will yield a value of S which is greater than 2. The maximum violation varies from system to system depending on the number of particle. This experiment will be dealing with 2 and 4-photon system with horizontal (H) or vertical (V) polarisation as measurement outccome. The main difference in the derivation lies in the average of the measurement outcomes $\overline{A}$ and $\overline{B}$.

2.2.1 2-PHOTON SYSTEM

For a 2-photon system, the state

$$\left|\psi^{-}\right\rangle = \frac{1}{\sqrt{2}}\left(\left|H,V\right\rangle - \left|V,H\right\rangle\right)$$

one of the four Bell's states is considered. The ket $|H,V\rangle$ means Alice and Bob obtain measurement outcome of H and V respectively and so on. Since there are only two possible outcomes for Alice and Bob, H or V, there is a one-to-one correspondence with a spin-$\frac{1}{2}$ system, e.g. H and V corresponds to $+\frac{1}{2}$ and $-\frac{1}{2}$ respectively. The average measurement outcome can then be written as

$$\overline{A}(\alpha,\lambda) = P(+\frac{1}{2}|\alpha,\lambda) - P(-\frac{1}{2}|\alpha,\lambda)$$
$$\overline{B}(\alpha,\lambda) = P(+\frac{1}{2}|\beta,\lambda) - P(-\frac{1}{2}|\beta,\lambda)$$

where $P(+\frac{1}{2}|\alpha,\lambda)$ is the probability of Alice obtaining measurement result $+\frac{1}{2}$ with analyser setting α and so on. From the quantum mechanical prediction, the correlation function between Alice and Bob's measurement outcome is written as

$$E(\alpha,\beta)^{QM} = P(+\frac{1}{2},+\frac{1}{2}|\alpha,\beta) - P(+\frac{1}{2},-\frac{1}{2}|\alpha,\beta) - P(-\frac{1}{2},+\frac{1}{2}|\alpha,\beta) + P(-\frac{1}{2},-\frac{1}{2}|\alpha,\beta)$$

where $P(+\frac{1}{2},+\frac{1}{2}|\alpha,\beta)$ is joint probability of Alice and Bob obtaining measurement outcome $+\frac{1}{2}$ and $+\frac{1}{2}$ with analyser setting α and β respectively and so on. The correlation is just is the average of the product of the measurement. To

obtain $P(+\frac{1}{2},+\frac{1}{2}|\alpha,\beta)$, the transformation matrix for the creation operator of a horizontally and vertically-polarised photon, $\hat{a}_h^+$ and $\hat{a}_v^+$ is considered.

$$\hat{a}_h^+{}' = \hat{a}_h^+ \cos\theta + \hat{a}_v^+ \sin\theta$$
$$\hat{a}_v^+{}' = -\hat{a}_h^+ \sin\theta + \hat{a}_v^+ \cos\theta$$

Operating $\hat{a}_h^+$ and $\hat{a}_v^+$ on the vacuum state $|0\rangle_{vac}$, the following is obtained

$$\left|+\frac{1}{2}\right\rangle' = \hat{a}_h^+{}'|0\rangle_{vac} = \cos(\theta)\left|+\frac{1}{2}\right\rangle + \sin(\theta)\left|-\frac{1}{2}\right\rangle$$
$$\left|-\frac{1}{2}\right\rangle' = \hat{a}_v^+{}'|0\rangle_{vac} = -\sin(\theta)\left|+\frac{1}{2}\right\rangle + \cos(\theta)\left|-\frac{1}{2}\right\rangle$$

Thus the unitary transformation matrix $\hat{U}$ is

$$\hat{U} = \begin{pmatrix} \cos\theta & -\sin\theta \\ \sin\theta & \cos\theta \end{pmatrix}$$

From $\hat{U}$, the joint probability is obtained to be

$$
\begin{aligned}
P(+\frac{1}{2},+\frac{1}{2}|\alpha,\beta) &= \left|\left\langle +\frac{1}{2}\right| \otimes \left\langle +\frac{1}{2}\right| \hat{U}_a \otimes \hat{U}_b \left|\psi^-\right\rangle\right|^2 \\
&= \left|\left\langle +\frac{1}{2}\right| \otimes \left\langle +\frac{1}{2}\right| \hat{U}_a \otimes \hat{U}_b \left(\left|+\frac{1}{2}\right\rangle \otimes \left|-\frac{1}{2}\right\rangle - \left|-\frac{1}{2}\right\rangle \otimes \left|+\frac{1}{2}\right\rangle\right)\right|^2 \\
&= \left|\left\langle +\frac{1}{2}\right| \hat{U}_a \left|+\frac{1}{2}\right\rangle \left\langle +\frac{1}{2}\right| \hat{U}_b \left|-\frac{1}{2}\right\rangle - \left\langle +\frac{1}{2}\right| \hat{U}_a \left|-\frac{1}{2}\right\rangle \left\langle +\frac{1}{2}\right| \hat{U}_b \left|+\frac{1}{2}\right\rangle\right|^2 \\
&= \frac{1}{2}\sin^2(\alpha-\beta)
\end{aligned}
$$

Similarly,

$$
\begin{aligned}
P(-\frac{1}{2},-\frac{1}{2}|\alpha,\beta) &= P(+\frac{1}{2},+\frac{1}{2}|\alpha,\beta) = \frac{1}{2}\sin^2(\alpha-\beta) \\
P(+\frac{1}{2},-\frac{1}{2}|\alpha,\beta) &= P(-\frac{1}{2},+\frac{1}{2}|\alpha,\beta) = \frac{1}{2}cos^2(\alpha-\beta)
\end{aligned}
$$

and therefore

$$
E(\alpha,\beta)^{QM} = -\cos(2(\alpha-\beta))
$$

The expression for S based on the quantum mechanical consideration is then

$$
S = \left|-\cos(2(\alpha-\beta)) - \cos(2(\alpha-\beta')) + \cos(2(\alpha'-\beta)) - \cos(2(\alpha-\beta))\right|
$$

After a 4 variable maximisation process, the maximum violation is obtained to be S = 2.82843 > 2 at $\alpha = 0^o$, $\beta = 22.5^o$, $\alpha' = 45^o$ and $\beta' = 67.5^o$.

2.2.2 4-PHOTON SYSTEM

For a 4-photon system, the maximally entangled state

$$|\psi\rangle = \frac{1}{\sqrt{3}}\left(|2H,2V\rangle - |HV,VH\rangle + |2V,2H\rangle\right)$$

is considered [13]. The ket $|2H,2V\rangle$ means Alice and Bob obtain measurement outcome of HH and VV respectively and so on. Since there is only three possible measurement outcome, VV or HV and VH or HH, there is a one-to-one correspondence with a spin-1 system e.g. VV, HV and VH and HH corresponds to -1, 0 and 1 respectively. Thus the average measurement outcome for Alice and Bob can be written as

$$\overline{A}(\alpha,\lambda) = P(1|\alpha,\lambda) - P(0|\alpha,\lambda) + P(-1|\alpha,\lambda)$$
$$\overline{B}(\alpha,\lambda) = P(1|\beta,\lambda) - P(0|\beta,\lambda) + P(-1|\beta,\lambda)$$

From the quantum mechanical prediction, the correlation function between Alice and Bob's measurement outcome is written as

$$E(\alpha,\beta)^{QM} = P(1,1|\alpha,\beta) - P(1,0|\alpha,\beta) + P(1,-1|\alpha,\beta) - P(0,1|\alpha,\beta) + P(0,0|\alpha,\beta)$$
$$- P(0,-1|\alpha,\beta) + P(-1,1|\alpha,\beta) - P(-1,0|\alpha,\beta) + P(-1,-1|\alpha,\beta)$$

To obtain $P(+1,+1|\alpha,\beta)$, the procedure is similar to that for the 2-photon case. Operating, $\hat{a}_h^+$ and $\hat{a}_v^+$ on the vacuum state $|0\rangle_{vac}$, the following is obtained

$$|1\rangle' = \frac{(\hat{a}_h'^{+})^2}{\sqrt{2}}|0\rangle_{vac} = \cos^2(\theta)|+1\rangle + \sqrt{2}\cos(\theta)\sin(\theta)|0\rangle + \sin^2(\theta)|-1\rangle$$

$$|0\rangle' = \frac{(\hat{a}_h'^{+})^2}{\sqrt{2}}|0\rangle_{vac} = -\sqrt{2}\cos(\theta)\sin(\theta)|+1\rangle + (\cos^2(\theta)-\sin^2(\theta))|0\rangle + \sqrt{2}\cos(\theta)\sin(\theta)|-1\rangle$$

$$|-1\rangle' = \hat{a}_h'^{+}\hat{a}_v'^{+}|0\rangle_{vac} = \sin^2(\theta)|+1\rangle - \sqrt{2}\cos(\theta)\sin(\theta)|0\rangle + \cos^2(\theta)|-1\rangle$$

Thus the unitary transformation matrix $\hat{U}$ is

$$\hat{\mathrm{U}} = \begin{pmatrix} \cos^2(\theta) & -\sqrt{2}\cos(\theta)\sin(\theta) & \sin^2(\theta) \\ \sqrt{2}\cos(\theta)\sin(\theta) & \cos^2(\theta)-\sin^2(\theta) & -\sqrt{2}\cos(\theta)\sin(\theta) \\ \sin^2(\theta) & \sqrt{2}\cos(\theta)\sin(\theta) & \cos^2(\theta) \end{pmatrix}$$

From $\hat{U}$, the joint probability is obtained to be

$$\begin{aligned} P(1,1|\alpha,\beta) &= \left|\langle 1|\otimes\langle 1|U_a\otimes U_b|\psi\rangle\right|^2 \\ &= \left|\langle 1|\otimes\langle 1|U_a\otimes U_b\left(|1\rangle\otimes|-1\rangle - |0\rangle\otimes|0\rangle + |-1\rangle\otimes|1\rangle\right)\right|^2 \\ &= \left|\langle 1|U_a|1\rangle\langle 1|U_b|-1\rangle - \langle 1|U_a|0\rangle\langle 1|U_b|0\rangle + \langle 1|U_a|-1\rangle\langle 1|U_b|1\rangle\right|^2 \\ &= \frac{1}{3}\sin^4(\alpha-\beta) \end{aligned}$$

Similarly,

$$P(1,0|\alpha,\beta)=\frac{1}{6}\sin^2[2(\alpha-\beta)]$$
$$P(1,-1|\alpha,\beta)=\frac{1}{3}\cos^4(\alpha-\beta)$$
$$P(0,1|\alpha,\beta)=\frac{1}{6}\sin^2[2(\alpha-\beta)]$$
$$P(0,0|\alpha,\beta)=\frac{1}{3}\cos^2[2(\alpha-\beta)]$$
$$P(0,-1|\alpha,\beta)=\frac{1}{6}\sin^2[2(\alpha-\beta)]$$
$$P(-1,1|\alpha,\beta)=\frac{1}{3}\cos^4(\alpha-\beta)$$
$$P(-1,0|\alpha,\beta)=\frac{1}{6}\sin^2[2(\alpha-\beta)]$$
$$P(-1,-1|\alpha,\beta)=\frac{1}{3}\sin^4[2(\alpha-\beta)]$$

and therefore

$$E(\alpha,\beta)^{QM}=\frac{1}{3}\{1+2\cos[4(\alpha-\beta)]\}$$

The expression for S based on the quantum mechanical consideration is then

$$S=\left|\frac{1}{3}\{1+2\cos[4(\alpha-\beta)]\}-\frac{1}{3}\{1+2\cos[4(\alpha-\beta')]\}\right.$$
$$\left.+\frac{1}{3}\{1+2\cos[4(\alpha'-\beta)]\}+\frac{1}{3}\{1+2\cos[4(\alpha'-\beta')]\}\right|$$

After 4 variable maximum process, the maximum violation is obtained to be S = 2.55228 > 2 at $\alpha = 0^{o}$, $\beta = 11.25^{o}$, $\alpha' = 22.5^{o}$ and $\beta' = 33.75^{o}$ [13].

2.3 EXPERIMENTAL VIOLATION OF BELL'S INEQUALITY

The values for the quantity S obtained above are theoretical maximums. In an actual experiment, various factors, e.g. noise, down-conversion and collection efficient, will degrade the quality of the entanglement and thus lower the maximum value of S obtained. One commonly used method to establish the degree of violation expected from an experimental setup is by looking at its' visibility. It involves fixing the measurement basis of one analyser and while varying the other. Typical examples of visibility measurements are shown in chapter 5.

To illustrate this connection between the noise, degree of violation and visibility for a 4-photon experiment, let's assume that the noise in the setup consists of a statistical mixture of sum of the individual components in the pure state and the pure state itself [13]. The resulting density matrix can be express as

$$\rho = p(|\psi\rangle\langle\psi|) + \frac{(1-p)}{3}(|2H,2V\rangle\langle 2H,2V| + |HV,VH\rangle\langle HV,VH| + |2V,2H\rangle\langle 2V,2H|)$$

where value p quantifies the relative magnitude of the noise with respect to the pure state and is also related to the lowest fringe visibility that can be obtained [13]. With the density matrix, the correlation function is evaluated to be

$$E(\alpha,\beta)=\frac{1}{3}\left(1+2p\cos(4(\alpha-\beta))\right)-2(p-1)\cos(4(\alpha+\beta))$$

Due to additional noise components in the input state, it is no longer rotationally symmetric. Thus the maximum value of S obtained is on longer dependent on the separation of the angles but also on the angle themselves. It is shown that for the maximum S, the angles must be distributed symmetrical around the optical axis of the down-conversion BBO [13]. Therefore the angles are such that intervals between them are equal, e.g. $\Delta\phi=\beta-\alpha=\alpha'-\beta=\beta'-\alpha'$. To determine the maximum visibility, one of the axes is fixed at the angle α at which the violation of S is the greatest. A plot of $\Delta\phi$ versus the value of S for various value of p or visibility is plotted. This is shown in Figure 1.

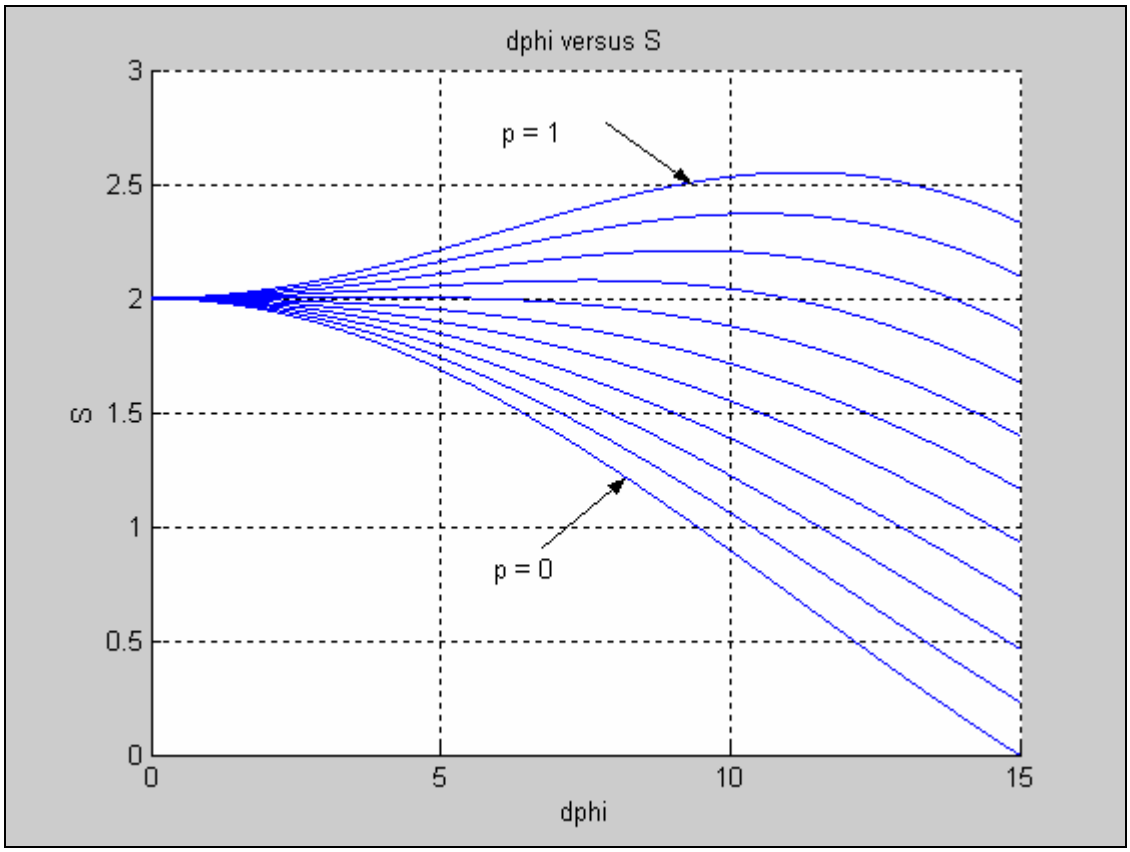

Figure 1 – $\Delta\phi$ versus S

Thus it can be seen that the visibility which is related to the value p will give an idea of the degree of violation one would expect.

2.4 LOOPHOLES IN OPTICAL BELL TESTS

Some of the Bell's inequalities including their applications in optical Bell tests are argued to be not full-proofed. There are a number of suggested experimental and theoretical loopholes that might bias these tests. This section briefly highlights a few of these suggested loopholes.

2.4.1 EXPERIMENTAL LOOPHOLE

FAIR SAMPLING

In experiment, for example the quantity $E(\alpha, \beta)^{QM}$ for the spin-$\frac{1}{2}$ system, is obtain by the following

$$E(\alpha,\beta)^{QM} = \frac{N(+,+) - N(+,-) - N(-,+) + N(-,-)}{N(+,+) + N(+,-) + N(-,+) + N(-,-)}$$

where each joint probability have been replaced with a ratio of the number of the specific coincidences to the total number of coincidences recorded in the same time interval. The fair sampling assumption states that the sample of the detected pairs is representative of all the pairs emitted. Detector efficiency and the size of the sample are two factors that may affect this assumption. Up to this point there is still no way of determining whether a sample is fair.

FAILURE OF ROTATIONAL INVARIANCE

The source is said to be "rotationally invariant" if all possible hidden-variable values are equally likely. While the derivation of the Bell's inequalities does not assume rotational invariance, experiments are sometimes analysed assuming this. It is possible that there has not always been adequate testing to justify this. Even when an actual general test is conducted, if the hidden-variables are not rotationally invariant, this can result in misleading descriptions of the results. For example, in looking at the dependence of coincidence rate on difference between the analyser settings, if a more

comprehensive set of experiments had been done it might have become clear that the rate depended on individual analyser setting separately [18].

SYNCHRONISATION PROBLEM

There are also reasons to think that in a few experiments bias could be caused when the coincidence window is shorter than some of the light pulses involved [18].

2.4.2 THEORETICAL LOOPHOLE

LOCALITY ASSUMPTION

The locality assumption is built into the derivation of the Bell's inequality. However there may be some unspecified mechanism whereby additional information is conveyed between the two detectors so as to increase their correlation above the classical limit. Though this is highly unlike given the many different geometry of experimental setups, some involving space-like separation between the two detectors.

Chapter 3
NONLINEAR OPTICAL EFFECTS

In this experiment, nonlinear optical crystals, Beta-Barium Borate (BBO), were used in the process of second harmonic generation (SHG) and parametric down-conversion (PDC). This chapter will detail the origin of this nonlinear optical phenomenon and how these effects can be used in frequency doubling and production of entangled photons

3.1 ORIGIN OF NONLINEAR OPTICAL EFFECTS

The electrons in a material are polarised when it is subjected to a weak electric field. For weak electric fields, the polarisation is linearly proportional to the externally applied field. For example,

$$\vec{P} = \varepsilon_0 \chi^{(1)} \vec{E}$$

where ε_0 is the permittivity of free space and $\chi^{(1)}$ is the linear susceptibility of the material. This linear susceptibility is related to the materials' refractive index. For crystalline materials, the linear susceptibility is a tensor that is related to the symmetry property of the crystal. For example, for an isotropic material, there is only one value for the index. Uniaxial crystals like the BBO used in this experiment, there are two values for the index, n_o and n_e for the ordinary and extraordinary indices of refraction. The

extraordinary direction is parallel to the optical axis of the crystal while the ordinary direction perpendicular to it. While for biaxial crystal, there are three values for the index and so on. The linear susceptibility is only just the first order approximation. The complete relation between polarisation and the applied field is an expansion in powers of the applied field. For example,

$$P = \varepsilon_0 \left(\chi^{(1)} E + \chi^{(2)} E^2 + \chi^{(3)} E^3 + ... \right)$$

where $\chi^{(2)}$ and $\chi^{(3)}$ are the second-order and third-order nonlinear susceptibility respectively. It is the second-order nonlinear susceptibility that is responsible for processes like second harmonic generation and parametric down-conversion.

3.2 SECOND HARMONIC GENERATION

In second harmonic generation, also known as frequency doubling, a single pump frequency ω is incident on a nonlinear medium and generates a wave at a frequency 2ω. This is illustrated in Figure 1.

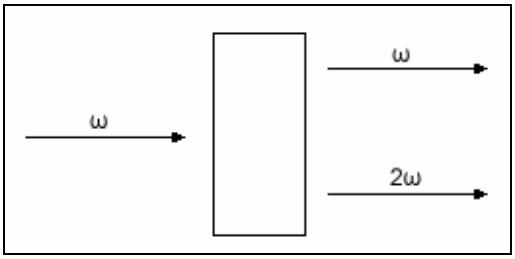

Figure 1 – Second harmonic generation

3.2.1 PROCESSES LEADING TO SECOND HARMONIC GENERATION

Essentially, the process of second harmonic generation can be understood as the modulation of the refractive index by an incoming electric field. The modulation is coupled to the electric field through the second order nonlinearity. The effect of this modulation in the material is to create side bands of various frequency which are the sum and differences of the pump frequencies.

3.2.2 CONVERSION EFFICIENCY

As a first order approximation to the derivation of the conversion efficiency in second harmonic generation [23], the pump power is assumed to be constant, thus giving rise to low conversion efficiency. The conversion efficiency is given by

$$\eta_{2\omega} = \frac{P_{2\omega}}{P_{\omega}} = \eta_{2\omega}^{0} \frac{\sin^2\left(\Delta kL/2\right)}{\left(\Delta kL/2\right)^2}$$

where $\eta_{2\omega}^{0}$ is the maximum conversion efficiency and ΔkL is the phase velocity. A plot of the above equation is shown in Figure 2.

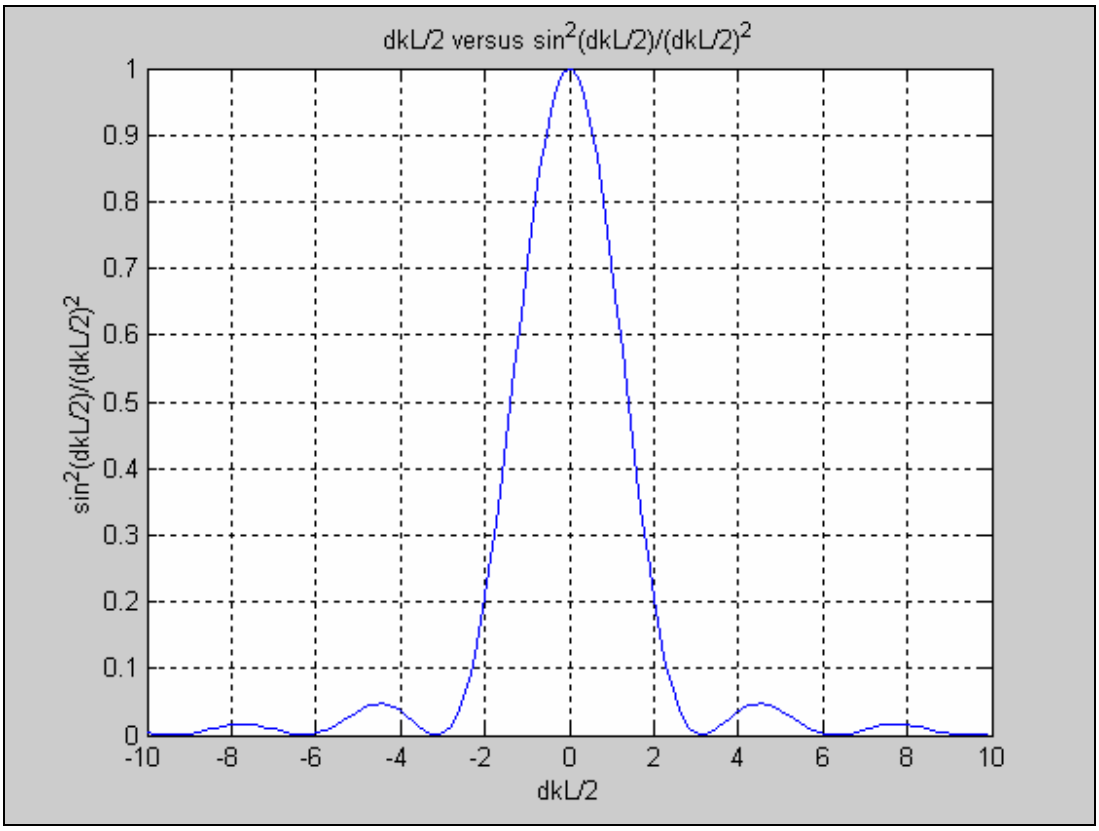

Figure 2 – Conversion efficiency with non-depleted pump assumption

From Figure 2 it can be seen that the conversion efficiency obtained with the non-depleted pump assumption has a sinc dependence on the phase velocity of the interacting wave. A small phase velocity mismatch will cause a significant drop in the conversion efficiency. This can be explained by appealing to the relative phase between the induced modulation and the pump. At the incident interface of the medium, the induced modulation and the pump are 180^{o} out of phase allowing maximum transfer of energy from the pump to the desired component. As the pump proceed through the medium, due to the mismatch in the phase velocity, the optimum phase relation at the incident interface of the materials begins to slip. This results in a drop in the conversion efficiency. After a

certain distance through the crystal, the phase shift is less than 90^{o}. This actually causes energy in the desired waves to flow back into the pump. As the pump wave continues to propagate, the energy will then flow back and forth between them.

Another related problem is that of the mismatch in the input phase. In ideal situation, the pump should have a zero phase shift at the incident interface of the medium. However, if there is a phase mismatch, the relative phase will not be constant and once again direction of the flow of the power will oscillate as the wave propagates. The period of this oscillation is shown to be dependent on the relative strengths of the wave intensities at the input [23]. This not only lowers the conversion efficiency but also affects the output mode of the desired component. For example, when a tightly focused pump beam is incidence on a nonlinear material, the change of intensity over the transverse profile of the beam is drastic. This will then set up oscillations in the direction of propagation of the pump power with different periods. The resulting non-uniform conversion efficiency will result in an output beam with a non-Gaussian mode.

3.2.3 PHASE MATCHING CONDITIONS (SHG)

It is clear from the previous discussion that in order for efficient second harmonic generation to occur, phase matching is necessary. Phase matching basically means matching the phase velocities of the desired wave and the driving wave. There are few types of phase-matching. In this experiment, the BBO crystals used are all cut collinearly for 800nm. In addition, they are placed at the waist of the pump beam. Thus only the

scalar angle phase-matching is considered. In scalar angle phase-matching, all the interacting waves are collinear.

For second harmonic generation, the phase-matching condition is

$$\vec{k}_w + \vec{k}_w' = \vec{k}_{2w}$$

For the collinear propagation, the phase matching condition reduces to

$$n_{2w} - n_w = 0 \text{ or } n_{2w} = n_w$$

Normally this cannot be satisfied as the refractive index generally increases with frequency. However for birefringent material, it is possible to do so. As mentioned earlier, for anisotropic material, there are two possible mode of propagation. In uniaxial crystals, one of these waves is the ordinary wave while the other is the extraordinary wave. The ordinary wave will encounter a constant refractive index, while the extraordinary wave will encounter a refractive index that is dependent on the direction of propagation. It is then possible to mix the two waves in anisotropic material so that the phase matching condition is satisfied. For example, in a negative uniaxial crystal where $n^o > n^e$,

$$n_w^o = n_{2w}^e\left(\theta_{pm}\right)$$

where θ_{pm} is the angle between the pump beam and the optical axis of the crystal. For a positive uniaxial crystal, $n^o < n^e$. There are two types of angle phase matching condition depending on the cut of the crystal. For type-I crystals, the two pump waves need to have the same polarisation while for type-II crystals, the two pump waves have orthogonal polarisation. Thus it can be seen that there are a few possible combination of pump polarisation and the polarisation of the resulting beam. For type-II, they are eeo and ooe. For type-II, they are eoe, eoo, oeo and oee. o and e refers to ordinary and extraordinary respectively. In uniaxial crystal, there is a single axis of symmetry, often referred to as the z-axis, which coincides with the optical axis. Therefore $n_x = n_y = n^o$ and $n_z = n^e$. The possible cases are shown in Figure 3 [23].

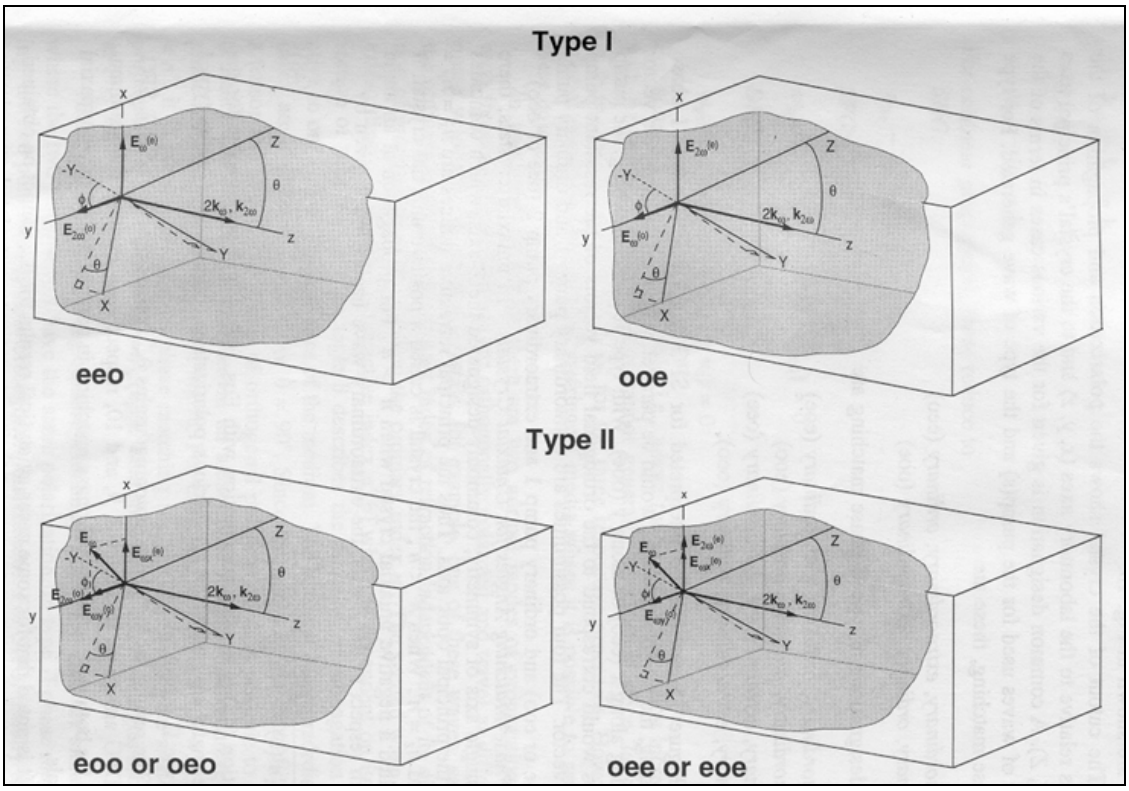

Figure 3 – Wave polarisation and direction of propagation

For propagation at an angle θ to the z-axis, the extraordinary wave relative index is given by

$$\frac{1}{n^e(\theta)^2} = \frac{\cos^2\theta}{(n^o)^2} + \frac{\sin^2\theta}{(n^e)^2}$$

Solving the above equation with the phase matching condition for the type 1 ooe case, the following is obtained.

$$\sin^2\theta_{pm} = \frac{\left(n_{2\omega}^{e}\right)^2}{\left(n_{\omega}^{o}\right)^2}\left[\frac{\left(n_{2\omega}^{o}\right)^2-\left(n_{\omega}^{o}\right)^2}{\left(n_{2\omega}^{o}\right)^2-\left(n_{2\omega}^{e}\right)^2}\right]$$

Thus the angle between the pump beam and the crystal axis at which phase matching condition can be satisfied is determined.

For the determination of n^o and n^e for the BBO crystal at various wavelengths, the following Sellmeier Equations [5] are used.

$$n_o^2 = 2.7359 + \frac{0.01878}{(\lambda^2 - 0.01822)} - 0.01354\lambda^2$$

$$n_e^2 = 2.3753 + \frac{0.01224}{(\lambda^2 - 0.01667)} - 0.01516\lambda^2$$

where λ is in μm. The Sellmeier coefficients are different for different crystals.

3.2.3 DETERMINATION OF THE CRYSTAL TILT ANGLE

When a crystal is said to be cut collinearly for a certain wavelength, it means that with the beam perpendicular on the incident surface of the crystal, the phase-matching condition is automatically satisfied. However, if the wavelength of the pump beam is

only close the wavelength for which it is cut collinearly for, it is possible to re-establish the phase matching condition by tilting the crystal.

In this experiment, the only available type-I BBO crystal available are cut collinearly for 800nm. Thus with a pump beam of 780nm, the crystal needs to be tilted With a pump beam of 780nm to be frequency doubled to 390nm the θ_{pm} is calculated to be 29.94^{o} with the previous mention method. For 800nm, θ_{pm} is calculated to be 29.18^{o}. Since there is a tilt in the crystal, the correction needs to be made to the difference of the two θ_{pm} due to refraction. Since the light from the laser used in the experiment is o-polarised, the refractive index used for the calculation of this correction is n^{o}(780nm) from the Sellmeier equation. The situation is illustrated in Figure 4.

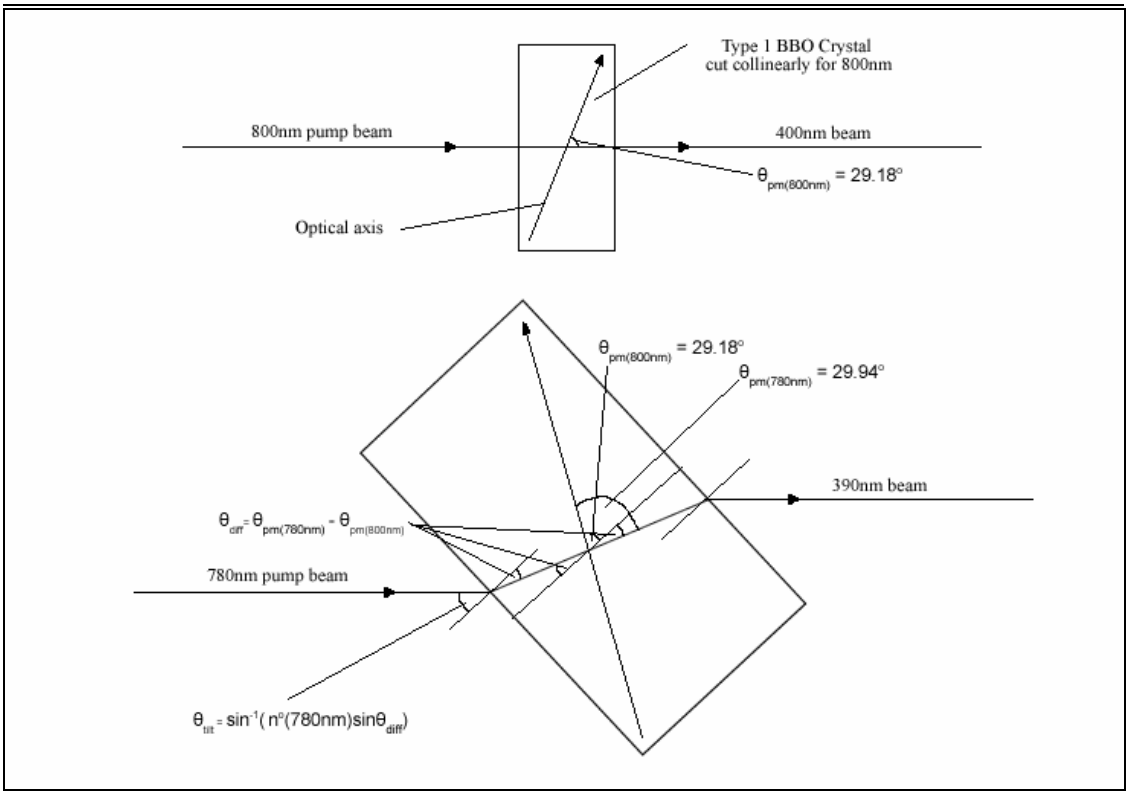

Figure 4 - Determination of the crystal tilt

Thus the calculation shows that the crystal needs be titled by 1.1817^{o} in order satisfy the phase matching condition for 780nm. From Figure 4 it can be seen that the 780nm beam will be deviated after frequency doubling. The direction of tilt must also correspond to the orientation of the crystal axis in order for the phase matching condition to be satisfied.

3.3 PARAMETRIC DOWN CONVERSION

Parametric down-conversion in a sense is the inverse of second harmonic generation. Whereas in the previous case two incident photons are use to generate one photon with twice the frequency, in the down-conversion process, one photon is incident on a non-linear medium and is 'broken' into two photon of lower frequency. This is illustrated in Figure 5.

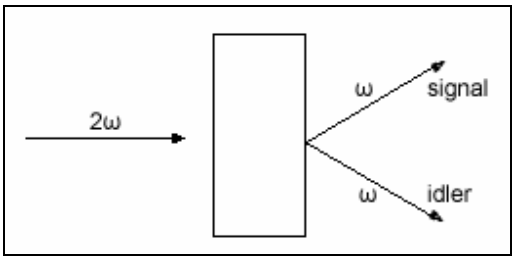

Figure 5 – Parametric down-conversion

3.3.1 PROCESSES LEADING TO PARAMETRIC DOWN-CONVERSION

Parametric down-conversion is a strictly quantum mechanical effect. To understand it a quantized field approach is used for the signal and idler fields, which interact via a perturbation Hamiltonian, based on the second order susceptibility $\chi^{(2)}$. The perturbation Hamiltonian is shown below.

$$g\left(\hat{a}_h^+\hat{b}_v^+ + e^{i\phi}\hat{a}_v^+\hat{b}_h^+ + h.c.\right)$$

where g is the coupling constant and h.c. is the Hermian conjugate of the first term

Thus the unitrary operator $\hat{U} = e^{-iH_I t}$

$$e^{-ig\left(\hat{a}_h^+\hat{b}_v^+ + e^{i\phi}\hat{a}_v^+\hat{b}_h^+ + h.c.\right)t}$$

Expanding $\hat{U}\left|0_{vac}\right\rangle$ in a power series, the following is obtained.

$$
\begin{aligned}
&|0\rangle - ig\left(\hat{a}_h^+\hat{b}_v^+ + e^{i\phi}\hat{a}_v^+\hat{b}_h^+\right)|0\rangle - \frac{g^2}{2}\left(\hat{a}_h^+\hat{b}_v^+ + e^{i\phi}\hat{a}_v^+\hat{b}_h^+\right)^2|0\rangle + \ldots \\
&= |0\rangle - ig\left(\hat{a}_h^+\hat{b}_v^+ + e^{i\phi}\hat{a}_v^+\hat{b}_h^+\right)|0\rangle - \frac{g^2}{2}\left(\hat{a}_h^+\hat{b}_v^+\hat{a}_h^+\hat{b}_v^+ + e^{i\phi}\hat{a}_h^+\hat{b}_v^+\hat{a}_v^+\hat{b}_h^+ + e^{i2\phi}2\hat{a}_v^+\hat{b}_h^+\hat{a}_v^+\hat{b}_h^+\right)|0\rangle + \ldots \\
&= |0\rangle - ig\left(|h,v\rangle + e^{i\phi}|v,h\rangle\right) - g^2\left(|hh,vv\rangle + e^{i\phi}|hv,vh\rangle + e^{i2\phi}|vv,hh\rangle\right) + \ldots
\end{aligned}
$$

The h.c. term is ignored as $\hat{a}|0\rangle$ and $\hat{b}|0\rangle$, acting the destruction operator on the vacuum state is 0. From the above, it can be seen the state $\frac{1}{\sqrt{2}}\left(|h,v\rangle - |v,h\rangle\right)$ and $\frac{1}{\sqrt{3}}\left(|hh,vv\rangle - |hv,vh\rangle + |vv,hh\rangle\right)$ comes out from the second and third term respectively when $\varphi = \pi$. This angle φ can be adjusted by tilting the down-conversion or compensator crystals. The strength of the coupling g is dependent on the pump power. Thus a higher pump power will favour the production of the $\frac{1}{\sqrt{3}}\left(|hh,vv\rangle - |hv,vh\rangle + |vv,hh\rangle\right)$ state. In addition, the pump duration needs to be short in order to ensure the entangled photons generated are from the second order down-conversion process rather than the first.

3.3.2 PHASE MATCHING CONDITIONS (PDC)

The phase matching condition for the parametric down-conversion is non-collinear. This is illustrated in Figure 6. It also depends on the type of cut. This is in turn related to the internal angle φ shown in Figure 3. For a type-I BBO, the angle φ is equal to 0^o while for type-II BBO this angle is 30^o. The main difference between the two types of cut is in the

direction of the emission cones for the o-polarised and e-polarised light. For a type-I crystal, there is two emission cones with axis collinear to each other. The light in the cones have the same polarisation. For a type-II crystal, the two emission cones are at an angle from each other. The light from one of the cones will be e-polarised while the other will be o-polarised. Normally type-II BBO crystals are cut collinearly for a certain wavelength. This means when the when light is collinear with it, the emissions cone will only be touching at one point. Thus to generate the degenerate state need in down-conversion experiment, the crystal is titled such that the two cones intersect at two points. This is illustrated in Figure 7.

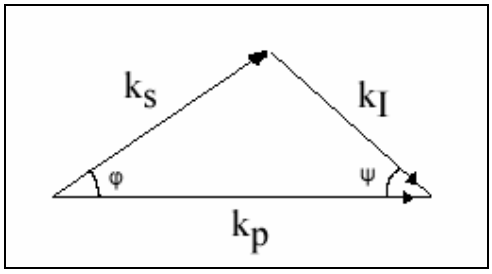

Figure 6 – Phase matching for PDC

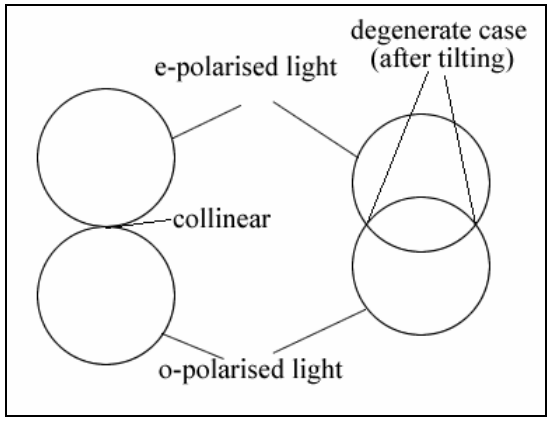

Figure 7 – Tilting the crystal to get degenerate case

Chapter 4
EXPERIMENTAL SETUP

In this experiment, the setup used is similar to that of the 2-photon entanglement experiment [15] with only a few exceptions. Firstly instead of a continuous-wave (cw) laser, a pulsed system is used for the generation of 4-photon entanglement. Secondly, there is an additional setup for frequency doubling thus also a need for a more elaborate set of correction optics to clean up the mode of the resulting beam. This chapter details the function of the various components of the setup, the techniques and procedures undergone in its' assembly.

4.1 BRIEF OVERVIEW OF SETUP

The first component consisted of a pulsed laser system operating at 780nm producing pulses of approximately 120fs wide at a frequency of 76MHz. The laser beam was directed to a straight path via two mirrors (useable wavelength range: 700nm to 1150nm) [20] and focused onto a type-I, 7x7x2mm BBO crystal where it was frequency doubled to 390nm. The resulting beam was then reflected 4 times off two dichoric mirrors (Reflecting: 300nm to 400nm, Transmitting: 600nm to 900nm) to remove any traces of the remaining 780nm component. Another mirror (useable wavelength range: 350nm to 400nm) [19] was then used to direct the resulting elliptical beam through a series of correction optics where it was focused onto type-II, 7x7x2mm BBO for parametric down-conversion. The down-converted light then passed through a half-wave plate and was directed by mirrors to a type-II, 7x7x1mm

BBO compensator crystals placed in each arm to correct for the temporal walkoff. This light was then collected by the collection optics and channelled through single-mode optical fibres to the analyser. The laser system was generating light with a polarisation approximately parallel to the surface of the optical table. Thus it was useful to define that direction as horizontal and the perpendicular direction as vertical. A diagram of the experimental setup is shown in Figure 1.

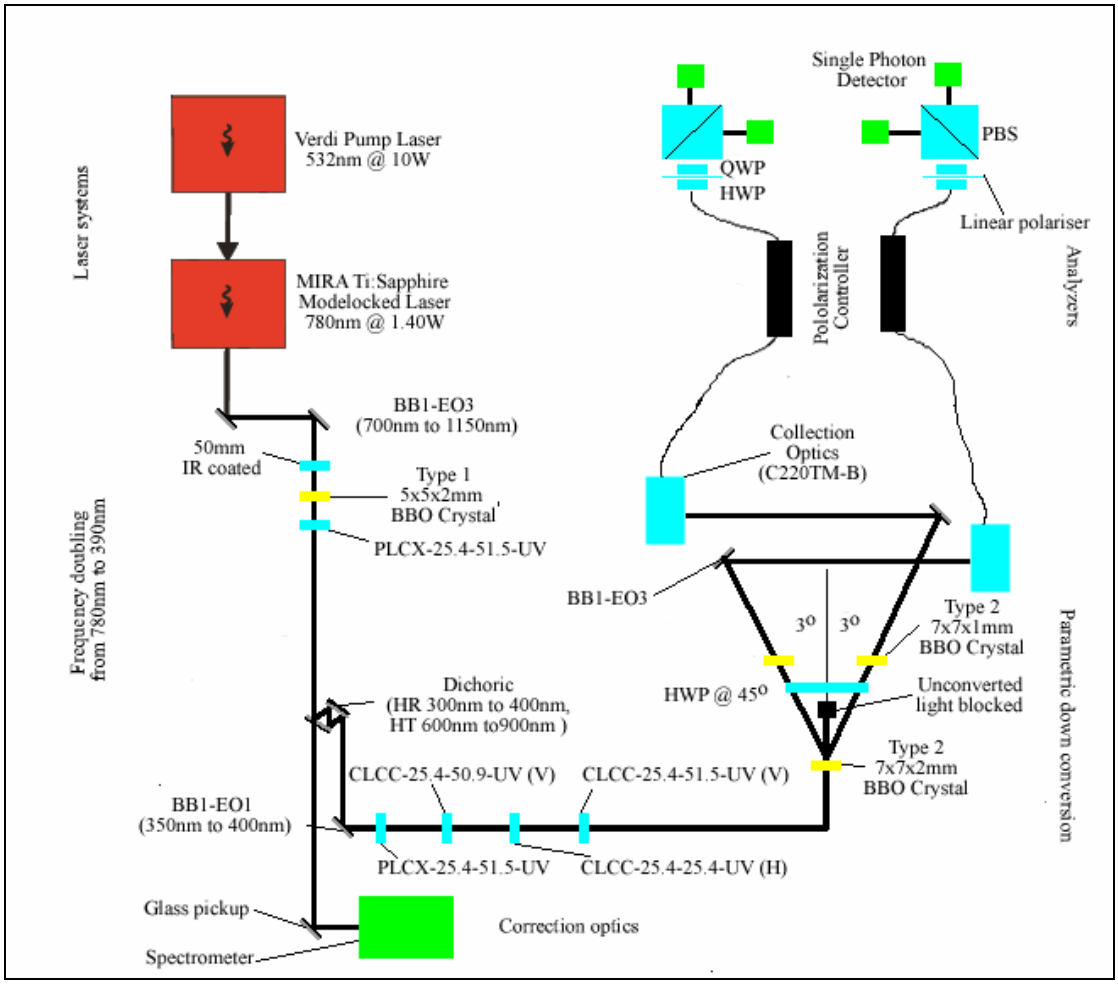

Figure 1 – Diagram for experimental setup

4.2 FREQUENTLY USED PROCEDURES

In the course of assembling the setup, two main procedures were frequently used. The first was waist measurements. Waist measurements were used to measure the profile of Gaussian beams; this is discussed in the Appendix. By measuring the profile of a beam at several positions along it, the waist and its' position could be determined. This information was then used to determine the correct placement of lenses. The second were the procedures used align various optical elements to the defined direction in the setup, specifically the horizontal and vertical direction.

4.2.1 WAIST MEASUREMENTS

Waist measurements were done by means of a knife-edge setup. This is shown in Figure 2. In the setup, a razor blade was mounted a motorised stage connected to a computer via a motor control card. During the measurement, the razor blade was moved in small steps, covering or uncovering the beam depending on the orientation. The intensity of the uncovered part of the beam was then measured using a photodetector connected to the computer via a data acquisition card. The photodetector circuit is shown in Figure 3. To avoid damage to the photodetector when measuring a high intensity beam, a glass slide was used as an optical pickup. Prior to the measurement, the resistance, R, was adjusted such that the output was not saturated when the whole beam was uncovered. The capacity, C, was included to filter out any noise. The time delay between the movement of the blade and the measurement was then set to be greater than the RC time constant of the circuit.

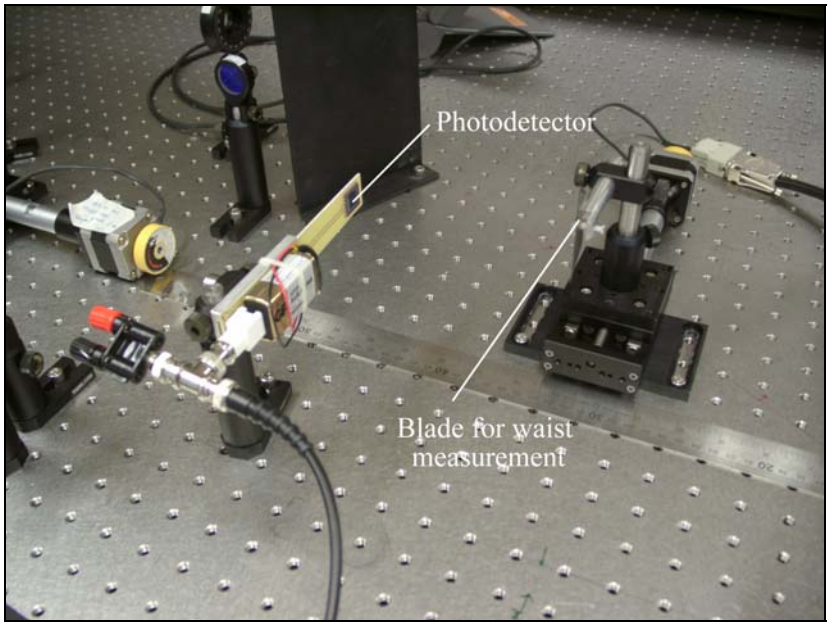

Figure 2 – A horizontal waist measurement

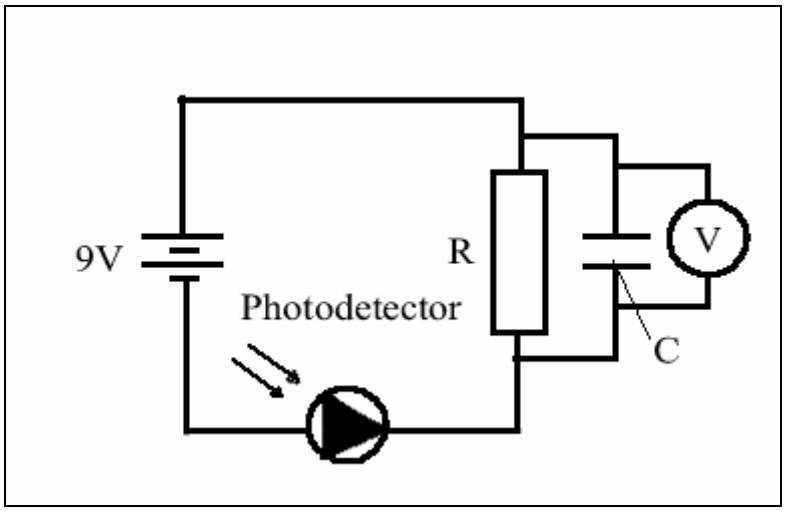

Figure 3 – Photodetector circuit

The measurements taken were fitted automatically to the error function to obtain the spot size of the beam. Several measurements of the spot size of a beam taken at different positions along it can be fitted to the beam-waist to determine the waist of

the beam and its' position. The same procedure was also used in vertical waist measurements except that the blade is mounted to move vertically.

4.2.2 ALIGNING VARIOUS OPTICAL ELEMENTS

In the experimental setup, the optical axis of elements like half-wave plates, linear polarisers and BBO crystals needs to be aligned with respective to the horizontal defined by the surface of the optical table. This was done by using Glan-Thompson polarisers (GT) which are aligned with respect to that direction; GT were used in this case as they could work over a large range of wavelength and provided better extinction in the ports. The action of a GT is shown in the Appendix. To align the GT, there was a need to for a source of horizontally and vertically polarised light that was defined with respect to the surface of the optical table.

Figure 4 shows the reflectance [17] for a BK7 substrate (n = 1.51 for 780nm) as governed by the Fresnel equation. It can be seen that for the p-polarisation, parallel to the plane of incidence, there exist an angle where the reflectance is zero. This is the Brewster's angle. Thus when randomly polarised light fell on the substrate at Brewster's angle, only the s-polarisation, perpendicular to the plane of incidence, was reflected. The s-polarised light was then used in the setup shown in Figure 5 for aligning the GT. Light from laser was directed through two pin holes set at the same height. This was to ensure the beam was straight and level. The beam was then reflected off the BK7 substrate. At Brewster's angle the intensity of the reflected beam should be the minimum as only the s-polarisation was reflected. Since the plane of incidence was well defined with respective the surface of the optical table, parallel to it, the s-polarisation was vertical. To align the axis of a GT to the horizontal, it was

placed in the path of the reflected beam. The GT was then rotated to minimise the light going through it. For vertical polarisation the GT was rotated to minimise the light coming out from the other port.

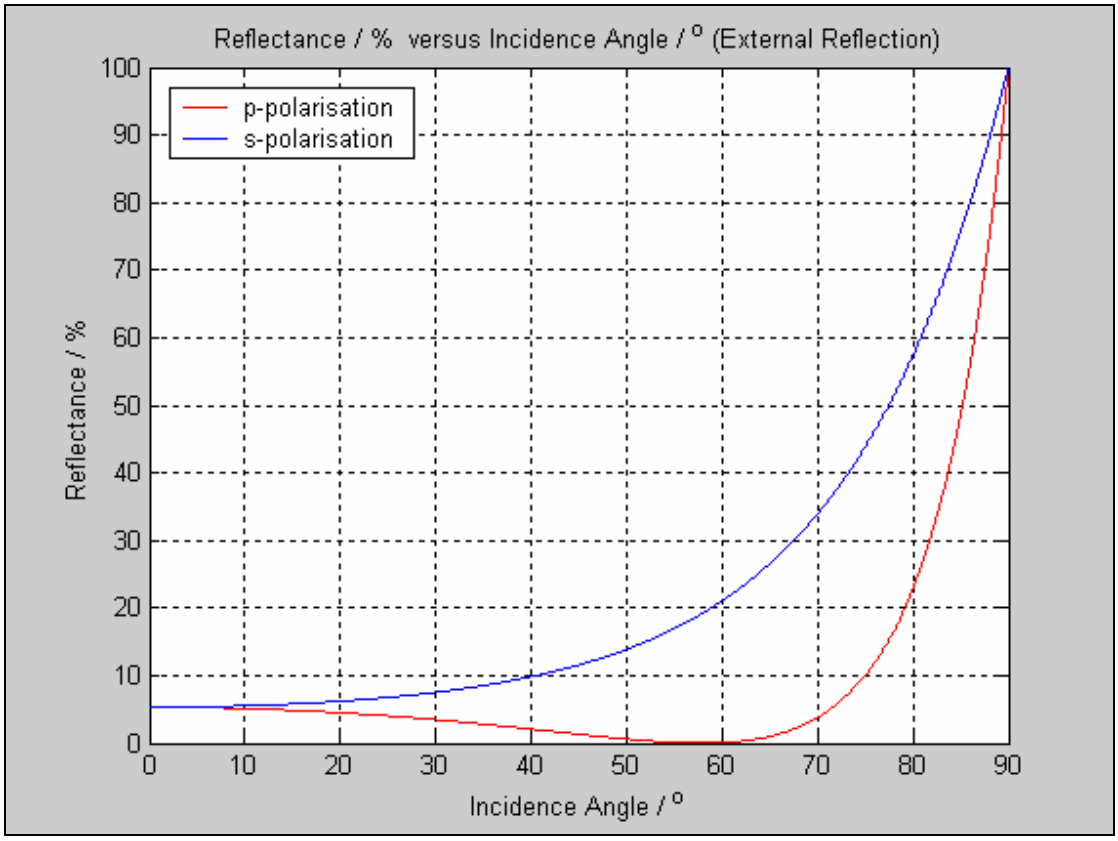

Figure 4 – Reflectance / % versus Incidence Angle / ° (BK7, External Reflection)

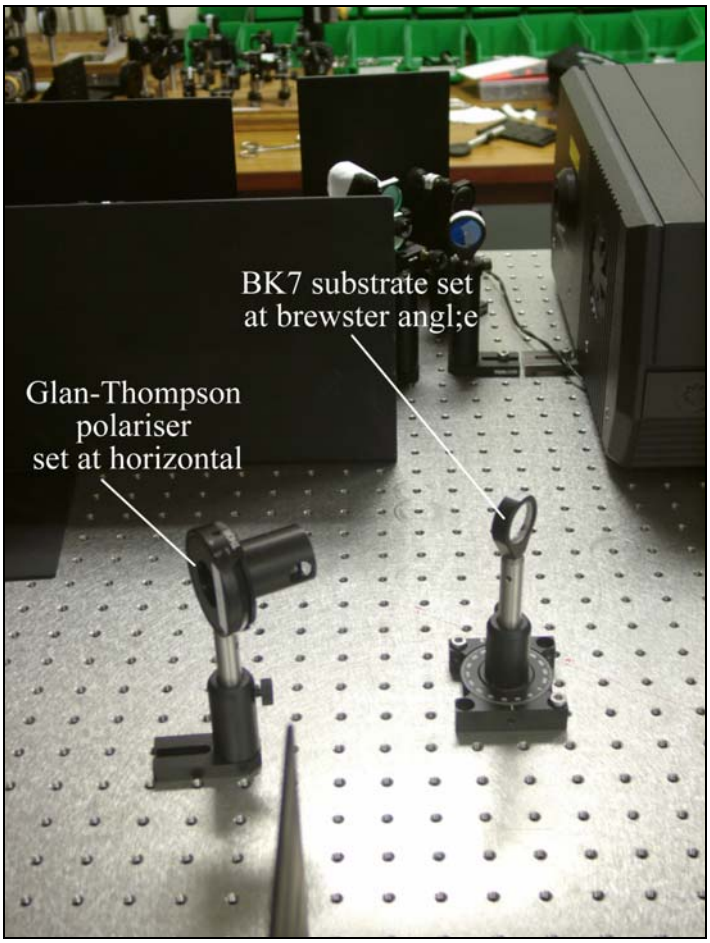

Figure 5 – Alignment of a Glan-Thompson polariser

Two GTs, one set to horizontal and the other set to horizontal or vertical were placed in line. The optical element could then be aligned by placing it in between them and rotating its' axis to minimise the light passing through to the second GT. For example, to align the optical axis of a half-wave plate to the horizontal, it was rotated to minimise the amount of light passing through the vertically set GT polariser. The setup is shown in Figure 6. The same was done to align the optical axis of a linear polariser to horizontal. To align a half-wave plate to 45^{o} to the horizontal, it was

.

placed in between two GTs set to horizontal and the light passing through them minimised by rotating the half-wave plate.

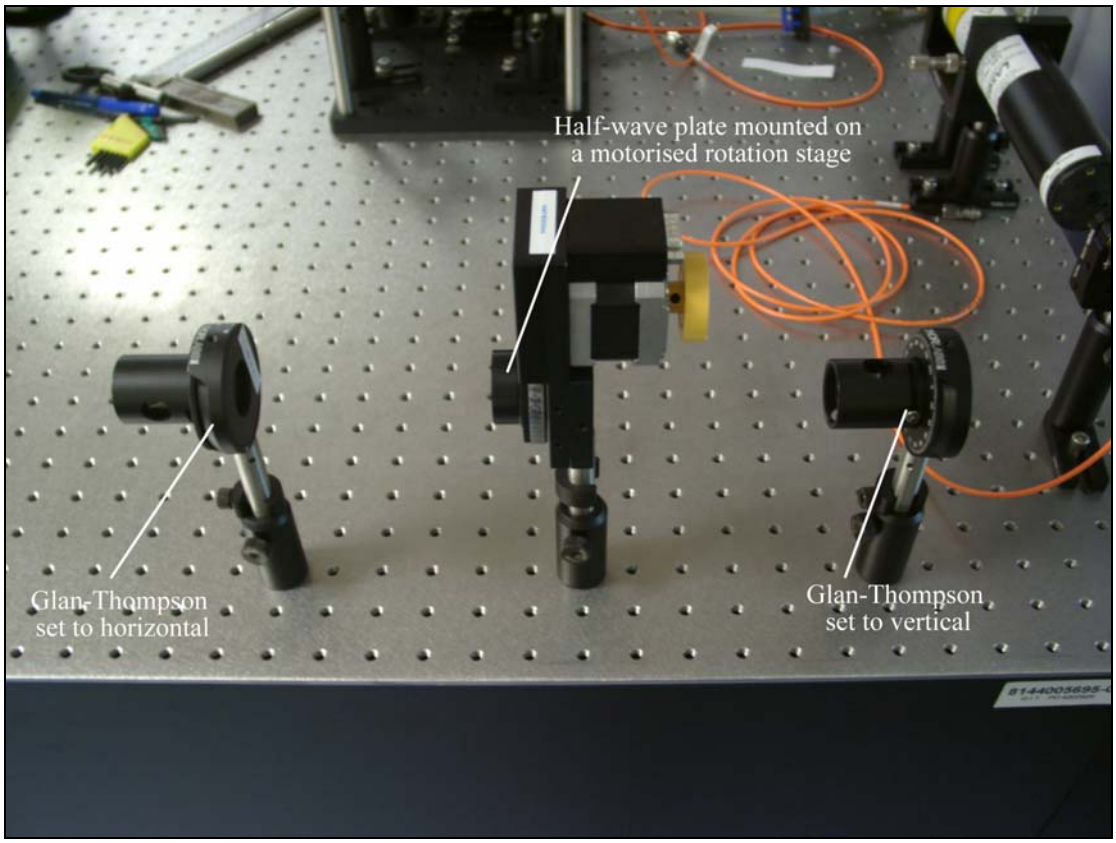

Figure 6 – Aligning the optical axis of a half-wave plate to the horizontal

4.3 THE MIRA AND VERDI LASER SYSTEM

The source of light in this experiment was a modelocked Titanium:Sapphire (Coherent MIRA-900F) laser pumped using light from a 532nm diode-pumped laser (Coherent Verdi V10). The laser system is shown in Figure 7.

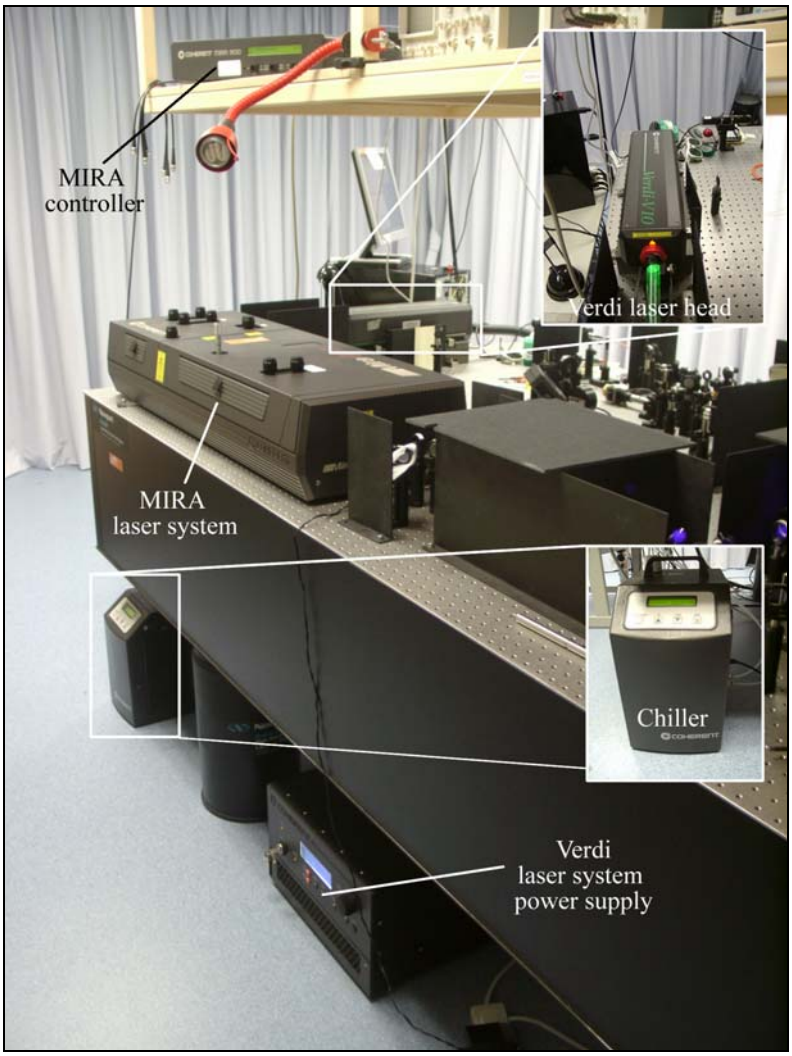

Figure 7 – The MIRA and Verdi laser system

The Verdi laser system consisted of two components, the laser head and the power supply. A schematic of the Verdi laser head is shown in Figure 8 [10]. The light source for the Verdi came from a series of laser diodes mounted in the power supply. The light was channelled to the laser head by means of optic fibers placed within the umbilical joining the two. In the laser head, the light was used to pump a Neodymium Vandate ($Nd:YVO_4$) crystal to produce 1068nm light. The 1068nm light was then

frequency doubled by a LBO crystal to 532nm. In this experiment, the Verdi power output was set to 10W.

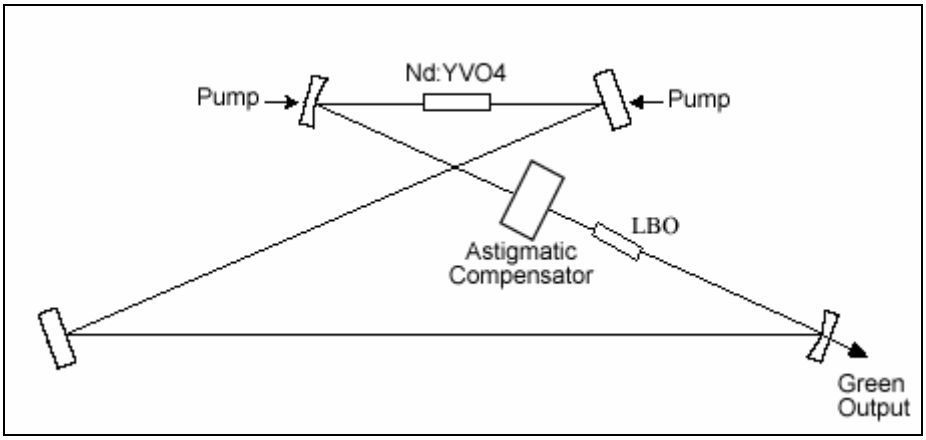

Figure 8 – Schematic of the Verdi laser system

The next important component in the setup is the MIRA laser system. A schematic of the MIRA laser system is shown in Figure 9 [9]. The MIRA generated pulses of light lasting about 120fs at a frequency of 76Mhz through a process called modelocking. The output coupler and flat end mirror M7 formed a cavity allowing only certain longitudinal modes to be supported within it. These modes consisted of different wavelength which satisfies the condition that an integral number of half wavelengths would fit in the cavity. When several of these modes were present simultaneously, they would add up randomly to produce intense pulses of light. To ensure the cw component was suppressed and that only the correct modes were present, the MIRA laser system used what was termed the optical Kerr effect in the Ti:Sapphire crystal. When a high intensity pulse passes through the Ti:Sapphire crystal, the associated electric field would distort the atom of the material causing a change in the refractive index. The non-uniform change in the refractive index causes

a lensing effect, reducing the profile of the beam. This beam with the reduced profile was then able to pass through the slit. For cw components or lower intensity pulses, the associated electric field was not strong enough to induce a lensing effect in the Ti:Sapphire crystal, thus their profile remains unchanged and were not able to pass through the slit. As a result, only the desired modes are locked together in the cavity. By adjusting the Brewster prism, P2 and birefringent filter, BRF, the temporal width and wavelength of the pulses can be changed.

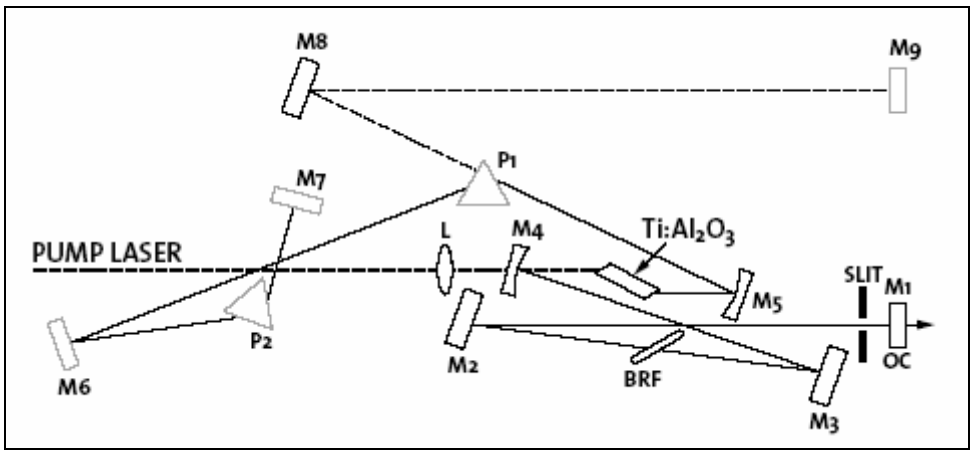

Figure 9 – Schematic of the MIRA laser system

After tuning the laser through the whole of its operating frequency, it was found that for a 10W pump, the top of the power tuning curve occurs at 780nm with a maximum output power of 1.40W to 1.50W. However at the initial stages of setting up the experiment, the power output from the MIRA was not stable and would degrade despite constant efforts at re-optimisation. Once the output power dropped below a certain point, the laser would not be modelocked properly. It was suspected that the problem was caused by excessive changes in the ambient temperature. In order to ascertain whether this was the case, the output power (measured by a photodetector

via a glass pickup) and ambient temperature over a 60 minutes period was measured. A plot of the data obtained is shown in Figure 10.

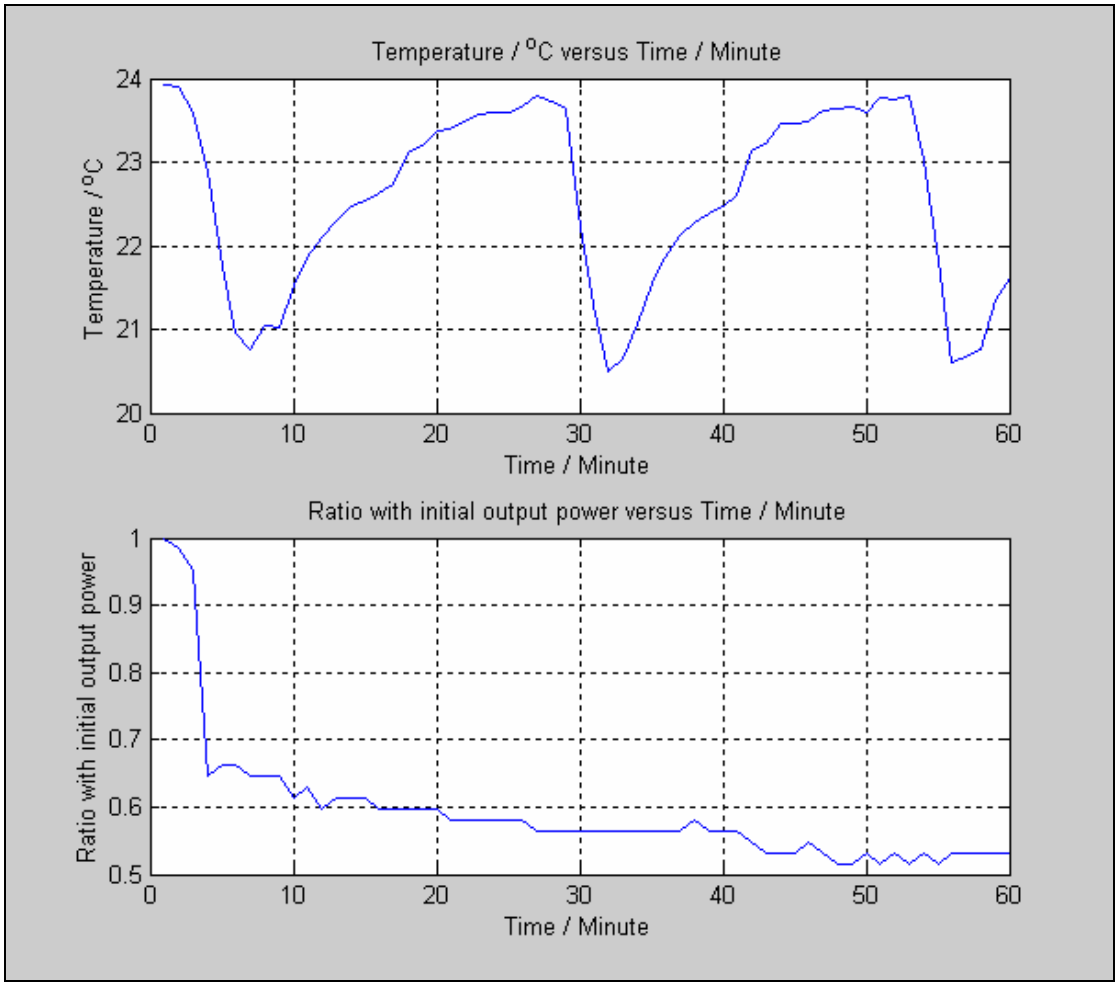

Figure 10 – Output power of laser and Temperature / °C versus Time / Minute (Old Location)

From Figure 10, the action of the thermostat can be seen. As the temperature rose to about 24°C, the thermostat of the air-condition arms, rapidly cooling the room to about 20.5°C. This temperature fluctuation of about 3.5°C cannot be compensated by the chiller and thus caused the instability in the MIRA. In the MIRA, the Ti:Sapphire crystal was pumped by the 532nm light from the Verdi laser. The input power was

10W while the output power at 780nm was about 1.40W to 1.50W. Most of the pump power was deposited as heat in the Ti:Sapphire crystal. The high temperature and its' differential in the crystal induced a non-uniform change in the refractive index. This introduced a thermal lensing effect. Thus when the surrounding temperature fluctuates drastically, the degree of thermal lensing would be changed affecting the stability of the laser. This problem was solved only after moving the setup to a new location where the ambient temperature is more stable. The same measurement of the ambient temperature over a period of 60 minutes was conducted there. A plot of the data is shown in Figure 11. The ambient temperature fluctuation is now less than 1^{o}C.

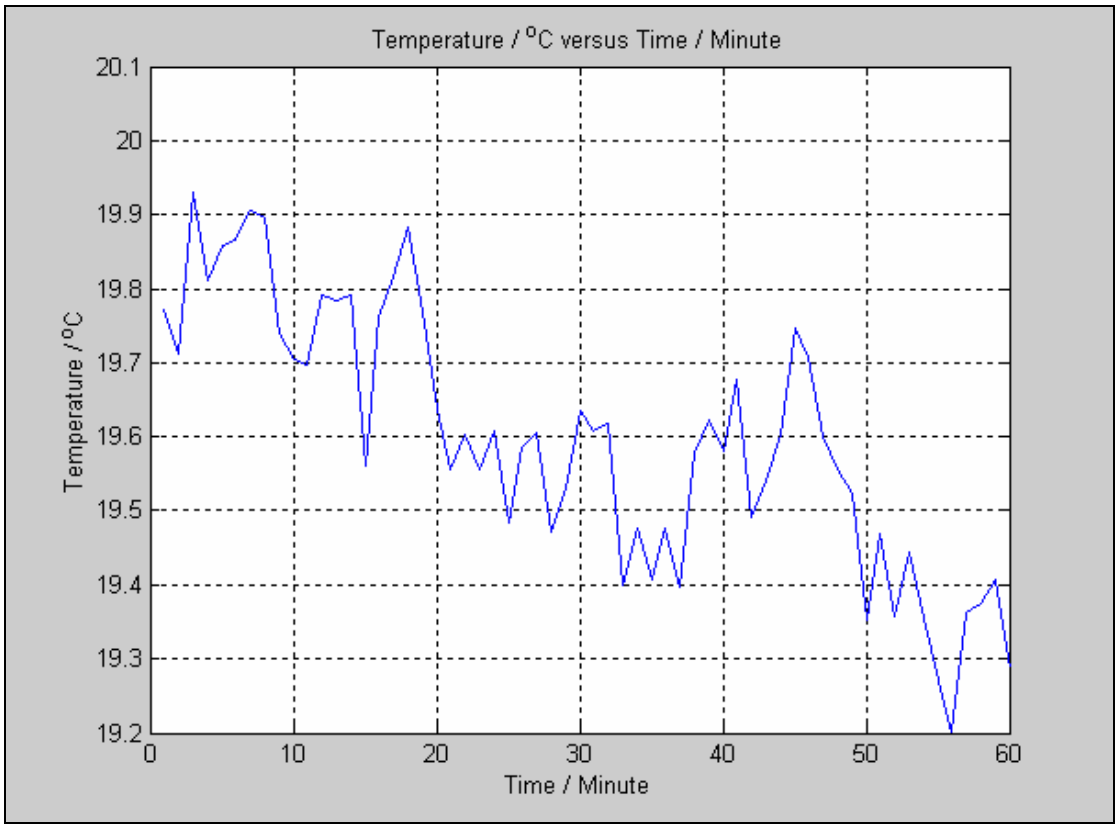

Figure 11 –Temperature / ^{o}C versus Time / Minute (New Location)

After the output power was optimised and verified to be stable, it was fed through two pin holes set at the same height via two mirrors. This was to ensure that the beam was both levelled with respect to the table and was travelling straight.

4.4 ALIGNING THE BBO CRYSTALS

In the setup there were four BBO crystals; one of them was used for frequency doubling and the other three for the down-conversion and compensation process. They must be mounted such that their optical axes were vertical with respective to the top of the optical table.

The first step in mounting the crystal was to identify the direction of the optical axis of the crystal. The procedure to identify the direction axis made use of the fact that BBO crystals are birefringent. For the procedure, a dot was first made on a piece of lens cleaning tissue using a marker and the crystal placed on it. The image of the tissue through the crystal was then observed under the microscope. Under the microscope, it could be observed that the image of the fibre of the tissue was split into two after passing through the crystal. The separation of the two images would be dependent on the thickness of the crystal in question. To determine whether the image was e or o-polarised, the crystal was rotated while holding the tissue stationary. At the centre of the microscope field, it could then be observed that one of the images will appear to orbit the other. The image at the centre would be the o-polarised image, while the other one would be the e-polarised image. The optical axis would then point from the o-polarised image to the e-polarised image. The process is explained in

Figure 12. The BBO was then mounted on a customised crystal holder and the direction axis clearly labelled.

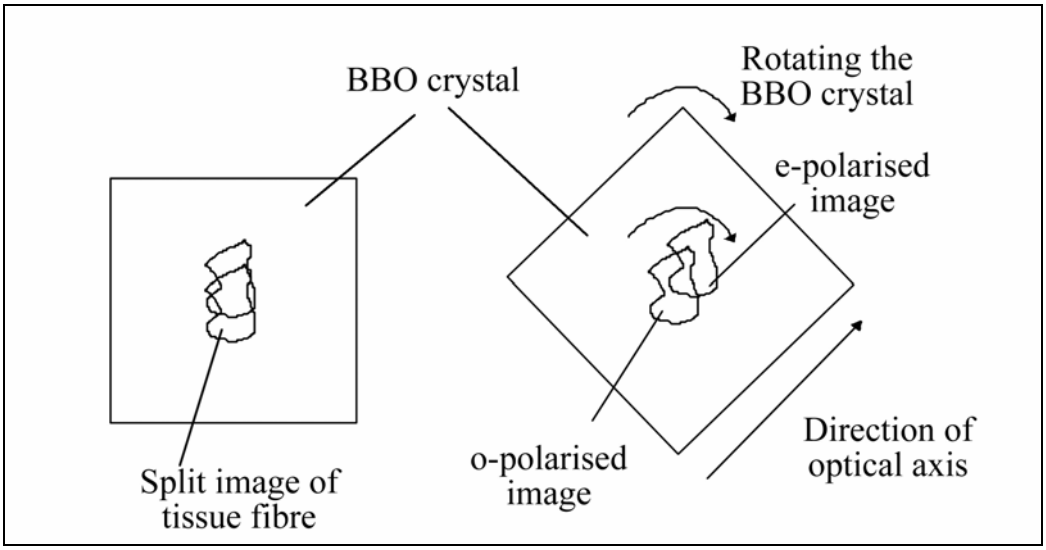

Figure 12 – Procedure to identify direction of optical axis

The second step was to mount the crystal on to a mirror holder while ensuring that the crystal axis was vertical with respective to the surface of the optical table. To do this, the mounted BBO crystal was placed between two GTs in the setup mentioned earlier. The setup used is shown in Figure 13. The optical axes of the two GT polarisers were set to horizontal and vertical respectively. Since the optical axes of the GTs were perpendicular, minimum amount of light should be observed through the second GT. The BBO crystals being birefringent would introduce a phase shift between the two perpendicular polarisations passing through it, thus rotating the direction of the polarisation. Therefore to ensure that the BBO crystal axis was vertical with respect to the table surface, the crystal holder was rotated in the mirror mount until the least amount of light was observed through the vertically set GT. The situation is illustrated in Figure 14.

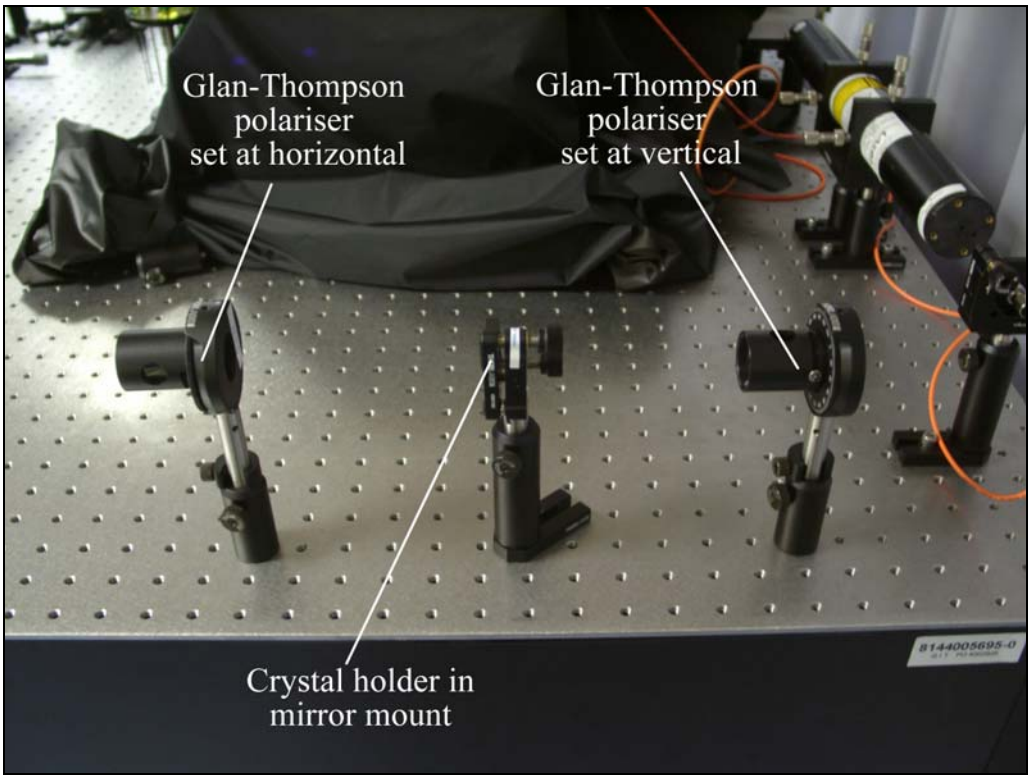

Figure 13 – Setup for aligning crystal holder in mirror mount

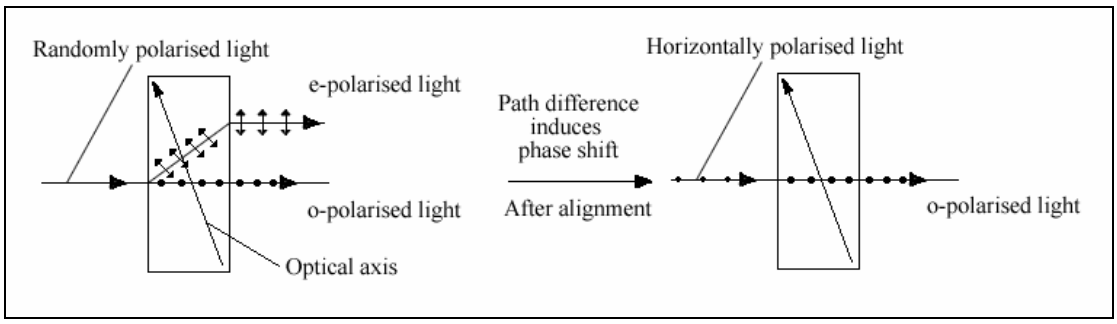

Figure 14 – Alignment of a BBO crystal

4.5 FREQUENCY DOUBLER

Before the down conversion process, the beam from the 780nm laser needs to be frequency doubled to 390nm. Initially, this was achieved with a commercial

frequency doubler using a LBO crystal. This is shown in Figure 15. However, after setting up the doubler a small distance behind the second mirror, it was found that the mode of the output was highly distorted and that the power degraded over time from its' initial value of approximately 500mW after re-optimisation. Shifting the doubler to approximately 10cm from the laser aperture and feeding the light directly into it improves the output mode, but the problem of the degrading power output still remains. Examination of the LBO crystal under the microscope revealed that it suffered some laser damage which was probably due to the certain conditions in the ambient surrounding. Thus the alternative of constructing a frequency double which utilises a BBO crystal is adopted.

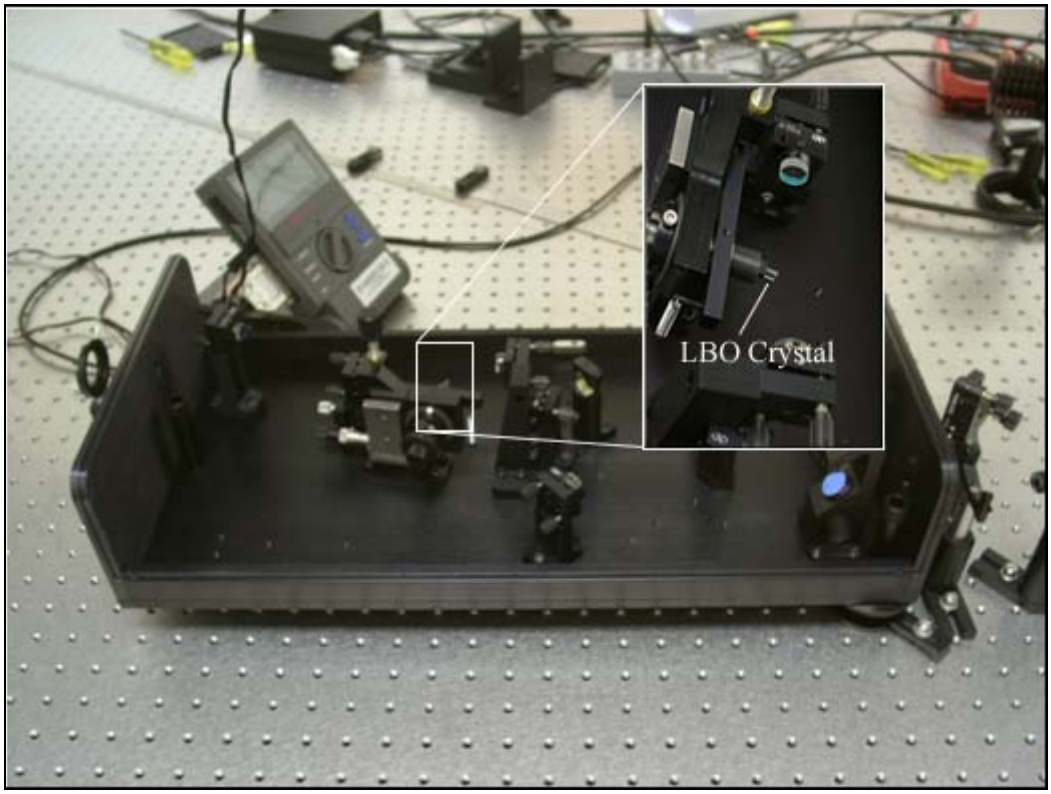

Figure 15 – Commercial frequency doubler with LBO crystal

The light from the laser was o-polarised. Thus the frequency doubling was achieved by passing the beam through a type-II BBO crystal under the ooe condition mentioned in Chapter 3. However, there was no type-II BBO that was cut collinearly for 780nm. The next closest choice was one cut collinearly for 800nm. Therefore to satisfy the phase matching condition, BBO crystal needs to be tilted. This is shown in Chapter 3 to be about 1.18^{o}. The amount of tilt was still acceptable and should introduce minimal distortion to the beam.

Initially a 5X5x0.3mm BBO crystal was chosen for the purpose. It was chosen so as not to cause further spreading in the temporal width of the pulse. After having chosen the crystal, the next step was to find the correct lens to focus the beam on to the crystal. To do this the beam-waist of the laser needs to be determined first. A reference point was defined a small distance behind the second mirror. Waist measurements was taken in order to find the beam-waist and its' position. The beam-waist was found to be 0.254mm at a distance -481.2mm from reference point. The fit is shown Figure 16.

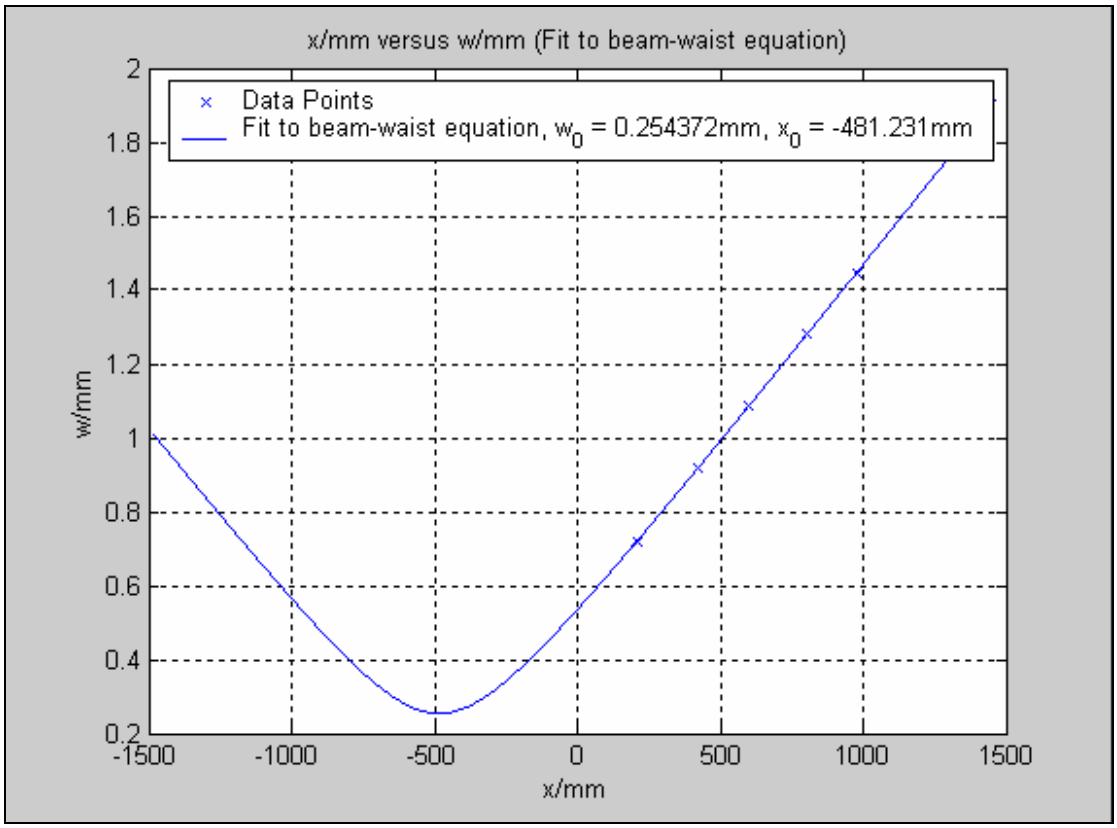

Figure 16 – Fit to beam-waist equation (pump laser)

Generally using a lens with a shorter focal lens, the conversion efficiently would be higher, as the beam was focused to a tighter spot. However due to the low angular acceptance of the BBO crystal, when the focal length was shorter than a certain limit, there would be a drop in efficiency. After a few trials with different lenses, it was found that the maximum output power obtained was only about 300mW, not nearly enough for the purpose of the experiment.

In addition there was also the occasional problem of back reflection from the crystal affecting the stability of the laser. Lasers work by inducing a resonance in an optical cavity. If there is back reflection from external elements, the cavity length is

essentially lengthened and stability of the beam will be affected. This problem was also observed when trying to couple a laser beam into a fiber. One attempt around this problem was to place a polarising beam splitter (PBS), followed by a quarter-wave plate (QWP) set at 45^{o} from horizontal. The setup is shown in Figure 17. The axis of the PBS was aligned to the polarisation of the laser so that the beam could pass through it un-deviated. This was then turned into circularly polarised light by the QWP. Any reflected light would pass through the QWP again to have its' polarisation rotated 90^{o} from that of the laser beam and be reflected by the PBS.

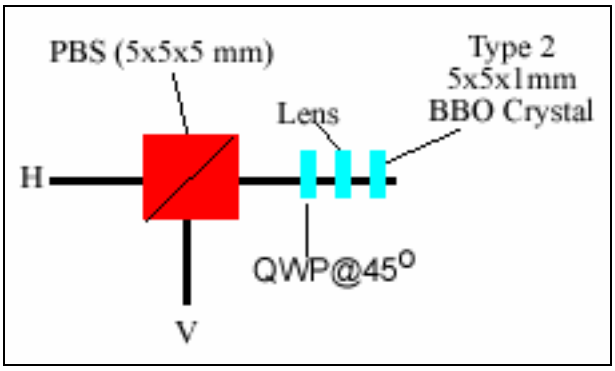

Figure 17 – Setup to prevent back reflection

As the light after the QWP was circular polarised, a type-II BBO crystal was used instead to satisfy the oee condition. The power output at 390nm observed with the setup was only about 200mW due to the lower nonlinearity coefficient as compared to that of the type-I BBO crystal. The beam splitter also needs to be small to prevent stretching of the beam pulse. However its' small size also made it prone to laser damage. Thus this setup was not implemented. Instead the focusing lens was tilted slightly to deviate the back reflection away from the laser aperture.

It was then later reasoned that since the down conversion crystal to be used was already 2mm in thickness, the use of a 2mm thick crystal for the frequency doubling should not stretch the temporal width of the pulse adversely. Thus a 7x7x2mm type-I BBO crystal was used for the purpose. It was observed that if a short focal length lens was used to focus the light to a tighter spot on the BBO, the output mode would not be Gaussian. This was due to the oscillatory nature of the power flow pump and the desired signal [23] mentioned in Chapter 3. The period of this oscillation was dependent on the input intensity. With a tight focus, the variation of the intensity over the beam is very drastic. This then causes visible differences in the conversion efficiency and thus the non-uniform intensity in the output mode. Thus the lens chosen should have a long enough focal length such that the input intensity was approximately uniform. After going through a few choices, it was found with the BBO crystal at the focus of a 50mm lens placed at 12mm from the reference point give the highest output power of about 800mW with the optimal output mode.

In order to further clean up the remaining 780nm component from the outgoing beam, it was reflected 4 times with dichoric mirrors (HR300-400nm, HT 600-900nm). In addition, as the focusing lens used had a relatively short focal length, the outgoing beam was too divergence to fit on the dichoric mirrors. Thus an additional 103mm focal lens was placed in front of the dichoric to make the beam less divergence. The setup is shown in Figure 18. The beam from the dichoric was then directed to the correction optics by a mirror.

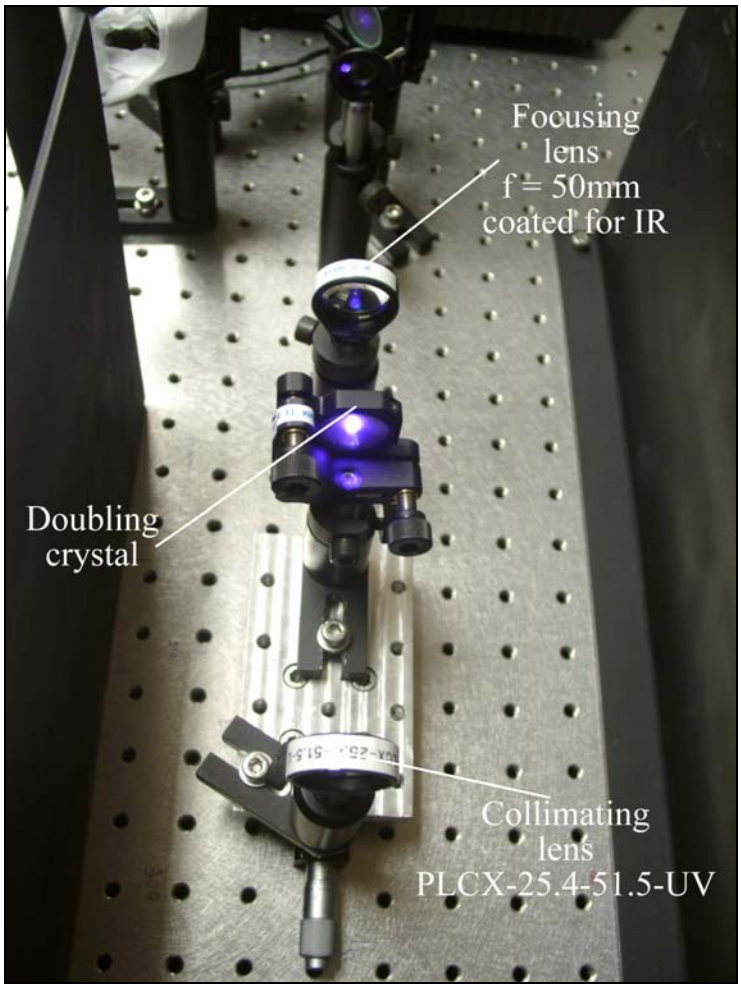

Figure 18 – Frequency doubling setup

4.6 CORRECTION OPTICS

Due to the birefringent nature of the BBO crystal, the resulting mode of the frequency doubled light is elliptical. A series of correction optics needs to be in place in order to get a circular beam with a waist of about 80μm at the position of the down-conversion BBO. This in turn had to be mapped optically to the collection mode of the collection optics. This was to ensure high efficiency in the collection process [14]. With another reference point defined just after the mirror behind the dichoric, a vertical and horizontal waist measurement was carried out. The vertical beam-waist was found to

be 23.4μm at about -701mm from the reference point. The horizontal beam-waist was found to be 82.6μm at about -3470mm from the reference point.

Based on the obtained value for the horizontal and vertical beam-waist, cylindrical lenses were placed in the path to get a circular beam of 80μm. However, the vertical beam-waist measurement of resulting beam did not correspond with that of calculation. This was probably due the fact that the beam was not diffraction limited. Therefore the position of the cylindrical lenses were gradually moved until its' waist was in the same as position as that of the horizontal component. Finally, with the configuration shown in Figure 19, a horizontal and vertical beam-waist measurement was again conducted to confirm the position of the waist. The fit to the beam-waist equation is shown in Figure 20. When the actual measurements were done at 600mm from the reference point, the beam was measured to have a vertical beam waist of 90μm and a horizontal beam waist of 84μm. This once again showed that the vertical component of the beam was not Gaussian. Even through the beam was not circular; the two waists are still within Rayleigh length of each other and thus should not adversely affect the coupling of the down-converted light to the collection optics.

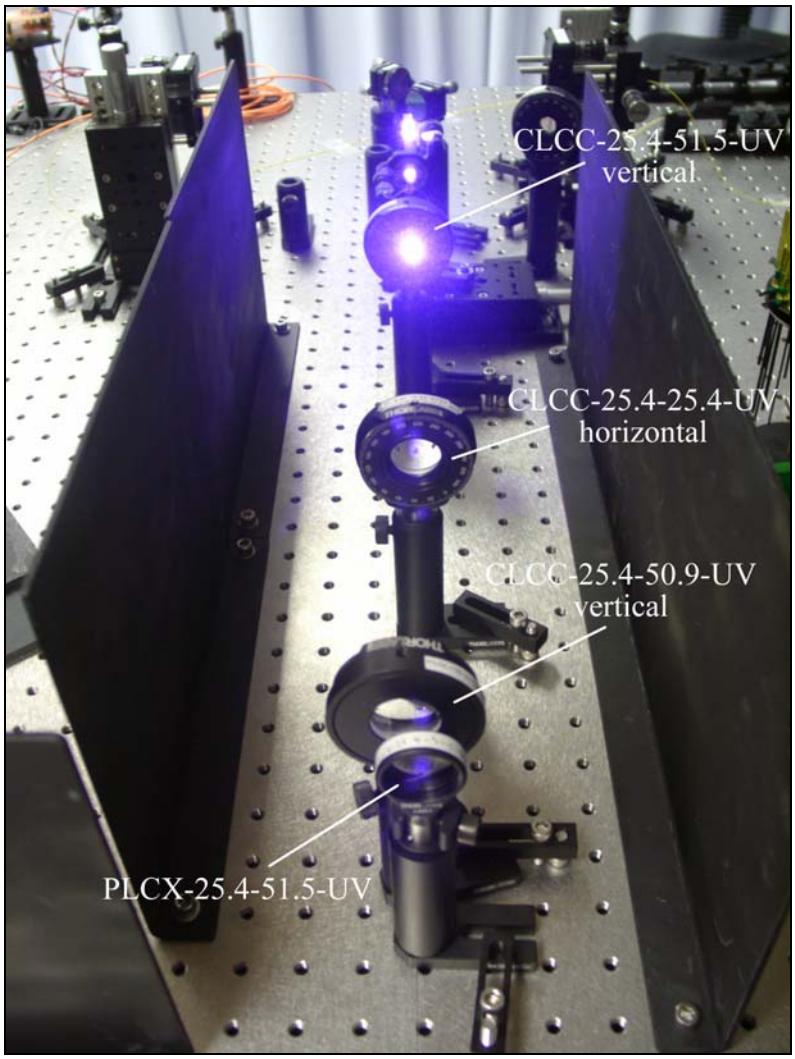

Figure 19 – Correction optics

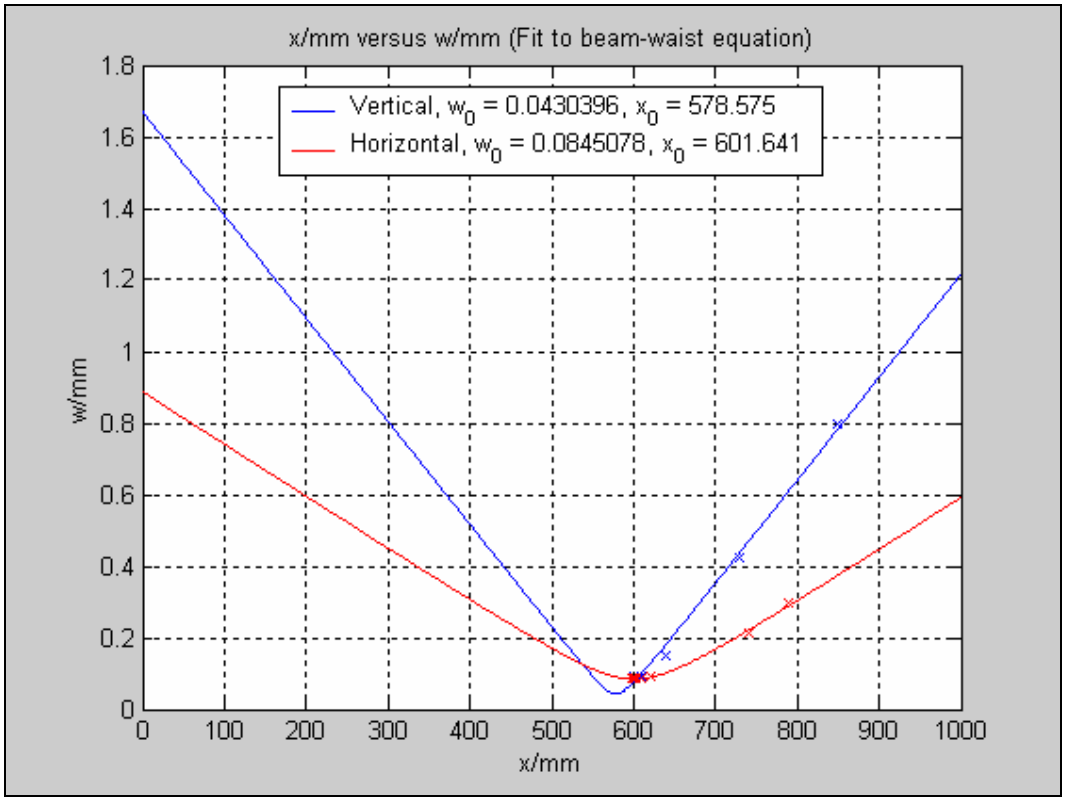

Figure 20 – Fit to the beam-waist equation

4.7 COLLECTION OPTICS

The down converted light is collected by the collection optics. This is shown in Figure 21. The collection optics used a focusing lens with an 11 mm focal length (anti-reflectance coated for 600nm to 1050nm [21]) placed on a Z translator to focus the collected 780nm down-converted light into the tip of a single mode fiber mounted on a XY translator. Single mode fibers were used in this case as the beam coming from the tip was Gaussian and that it changes the polarisation of the light in a predictable way. To ensure a good coupling between the down converted light and the collection

optics, the beam-waist of the collection mode needs to be also 80μm at the down-conversion crystal. This was done by passing light from a 785nm laser diode into the fiber and determining the resulting beam-waist and position from the base. The wavelength of the light used to determine the waist of the collection modes needs to be close to 780nm as the waist and its' position is dependent on the wavelength used.

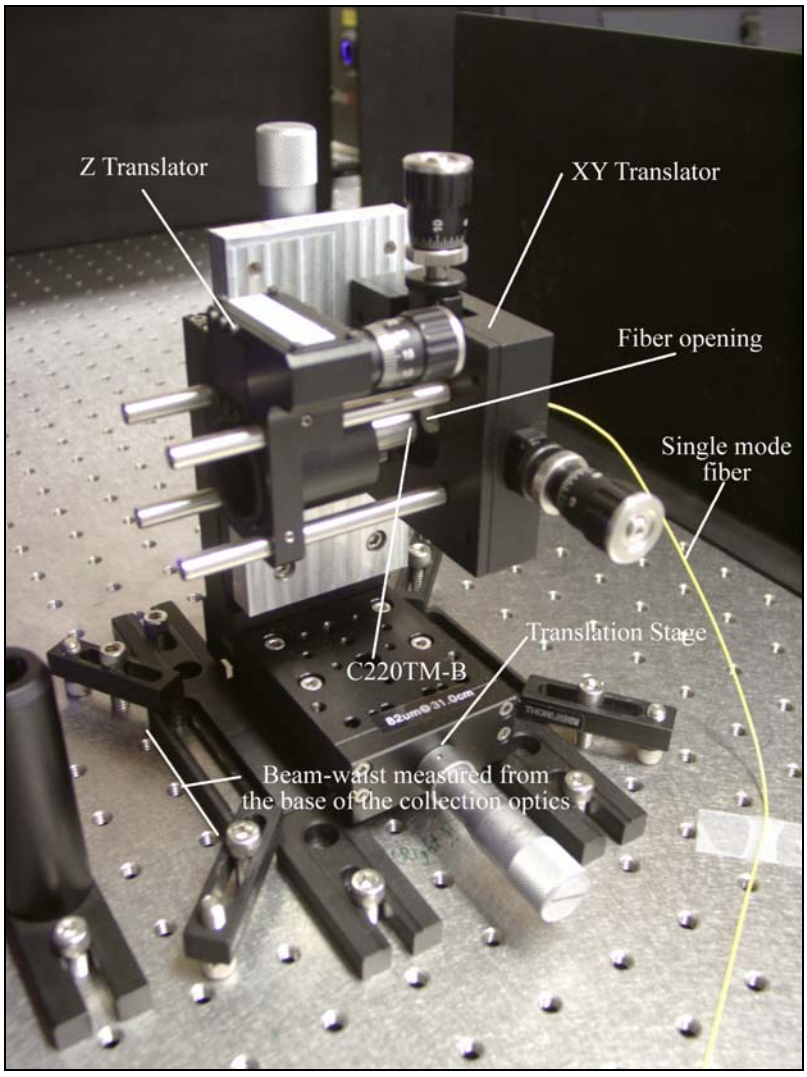

Figure 21 – Collection optics

In order to ensure the beam was straight and level, the XY translator and the translation stages were adjusted such the out-going beam passes through two pin holes set at the same height. The XY translator was then shifted until the focus was about 30cm from the base of the collection optics. Small adjustments were then made by to the position of the lens using the Z translator. After every adjustment, 5 spot size measurements were made along the path of the beam. The results were then fitted to the beam-waist equation to establish the beam-waist and its' position from the base of the collection optics. The fitted curves are shown in Figure 22. The beam-waist of the left and right collection optics were found to be about 84μm and 81μm at 30.6cm and 30.9cm from the base of the collection optics respectively.

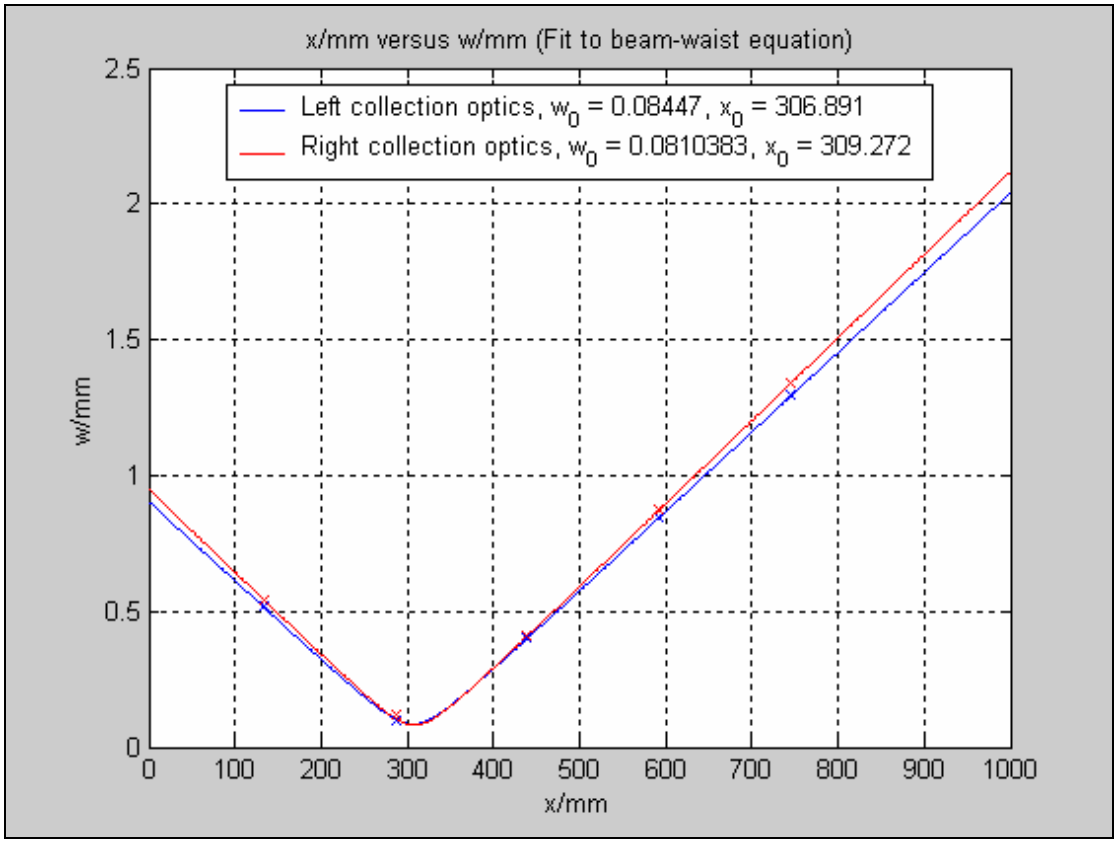

Figure 22 – Fit to beam-waist equation (collection optics)

The next step involved finding the correct placement of the collection optics and the two mirrors such that the down converted light from the degenerate case was collected at an angle of 3^o from path of the pump beam. The approximate geometry of the placement was first marked out on the optical table. To ensure that the collection mode of each collection optic was straight after the mirrors, light was sent into the collection optics through the fiber and their position adjusted so that the beam passes though two pin holes, set at equal height, placed along the straight section of the path. Pin holes were then placed on the 3^o line and the mirrors adjusted so that the beams from the collection optics pass through them.

Spot size measurements were then done at the approximate position of the waist of the pump beam. Small adjustment was made using the translation stage to locate the precise position waist of the pump beam. This is shown in Figure 23. After the precise position of the waist of the pump was located, the blade was left in place and the photodetector moved to the opposite side of the blade to measure the waist of the light from the collection optics. The collection optics was then translated in the direction of the path marked out on the optical table until waist fell on the position of the blade. This ensured that the beam-waist of the pump beam and the collection mode of the collection optics fell on the same position.

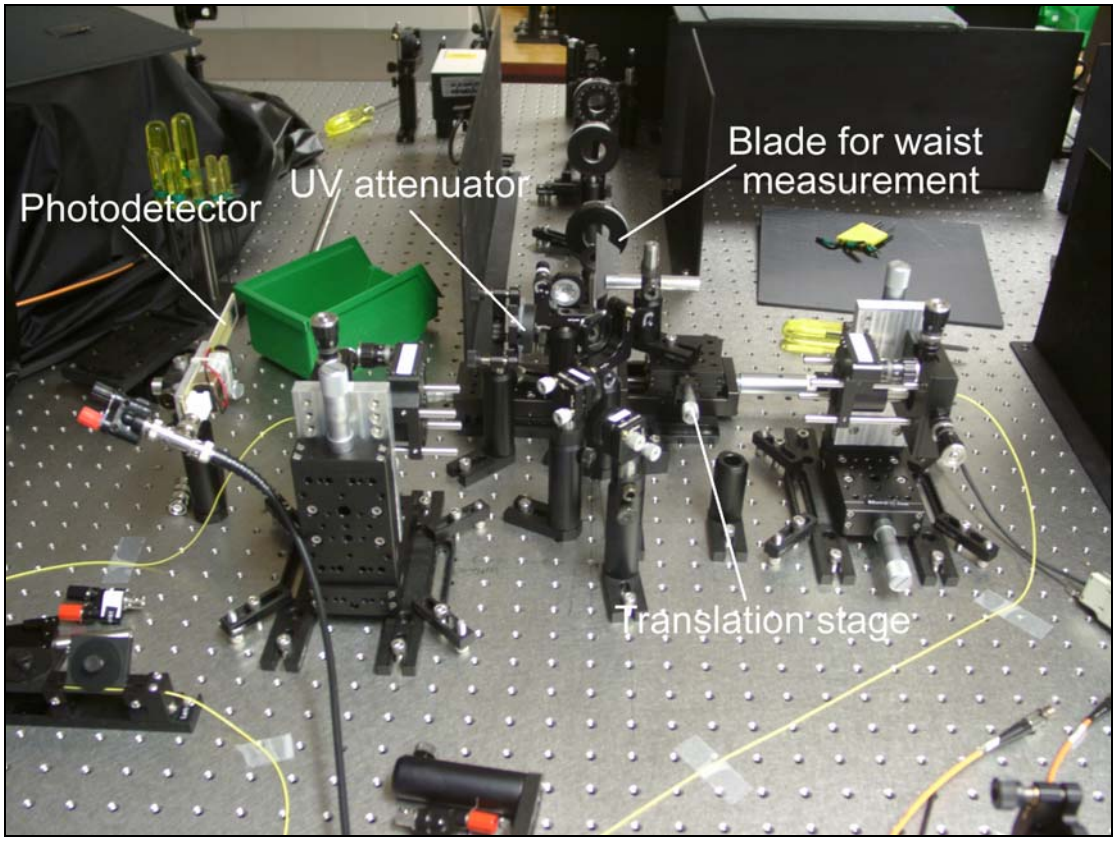

Figure 23 – Collection optics placement

4.8 ANALYSER

The photons collected by the collection optics were channelled via single-mode optical fiber to the analyser where their polarisation could be measured in different basis. Each analyser consists of three 11mm lenses, one for collimation and two for collection at each of the output port of the PBS. A stacked half-wave plate (HWP), linear polariser and QWP were placed in front of the PBS. The setup is shown in Figure 24.

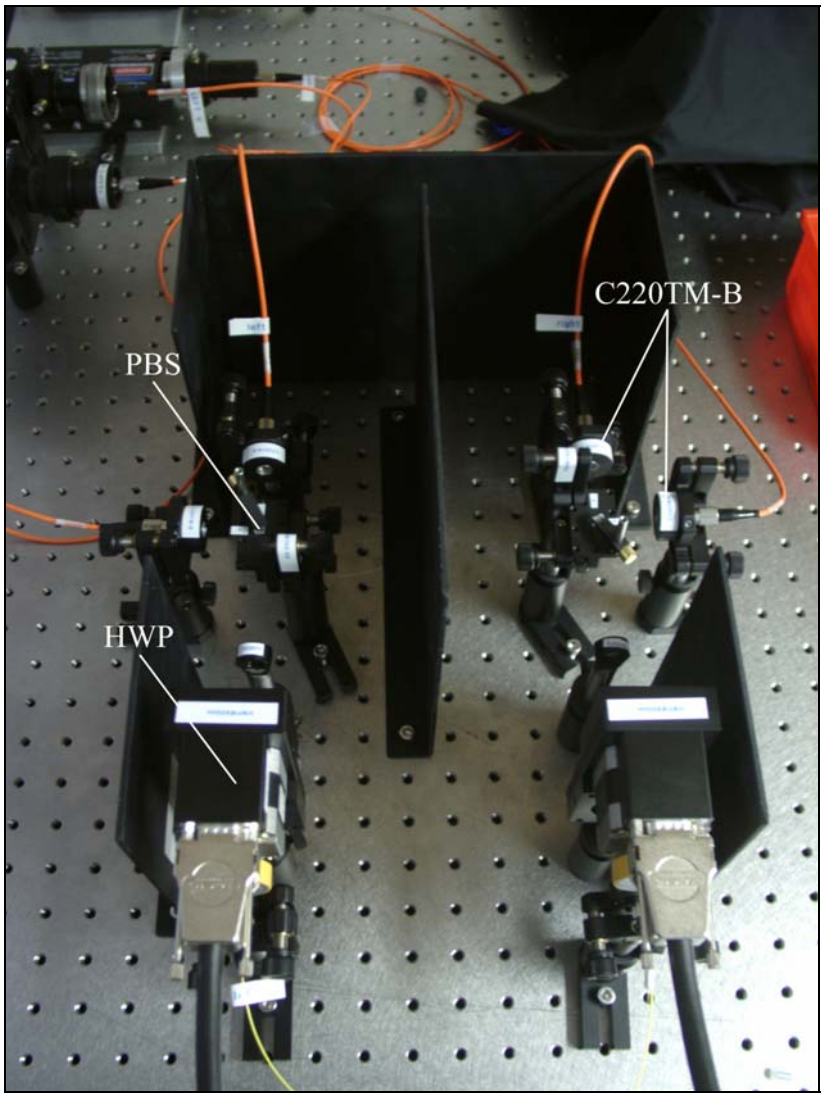

Figure 24 – Analyser setup

To ensure that the PBSs were well aligned, light from a 785nm laser diode was sent through the analyser. The PBSs were then adjusted such that the light from the second output port passes through pin holes placed perpendicular to the axis of the analyser. This ensures that axes of the PBSs were aligned to the surface of the optical table. As this was a 4-photon experiment, there was a need to distinguish state like HV or VH in each arm. Thus the output mode from both ports must remain as undistorted as possible to ensure high detection efficiency. This is why a GT was not used.

However, with the HWP and PBS alone, the analyser would not be able to distinguish state like $|HH\rangle$ and $|VV\rangle$. This was because the single photon detectors were not able to measure the number state of the collected photons. There were a few non-deterministic way solving this problem. The first method involved placing a quarter-wave plates set at 45^{o} in front of the PBS [13]. The QWP turns the horizontal or vertically polarised light into circularly polarised light. When the circularly polarised light passes through the PBS, half the time it would be split and exit at different ports. To select which state to measure, a linear polariser is placed front of the QWP to allow only the $|HH\rangle$ or $|VV\rangle$ state to enter. The second method involved placing 50:50 beam splitters at the each output port of the PBS. Similarly the HH and VV polarised photon would split into different output ports half of the time. The setup is shown in Figure 25. As mentioned these two methods were non-deterministic way of distinguishing the two states and works only about half of the time. Thus prior to the experiment, it is necessary to quantify the efficiency of detecting $|HH\rangle$ or $|VV\rangle$ state in each of the analysers. This detection efficiency is then use in the correction of the actual counts obtained. The HWP, QWP and compensator crystals can also be used in conjunction to reproduce any output state.

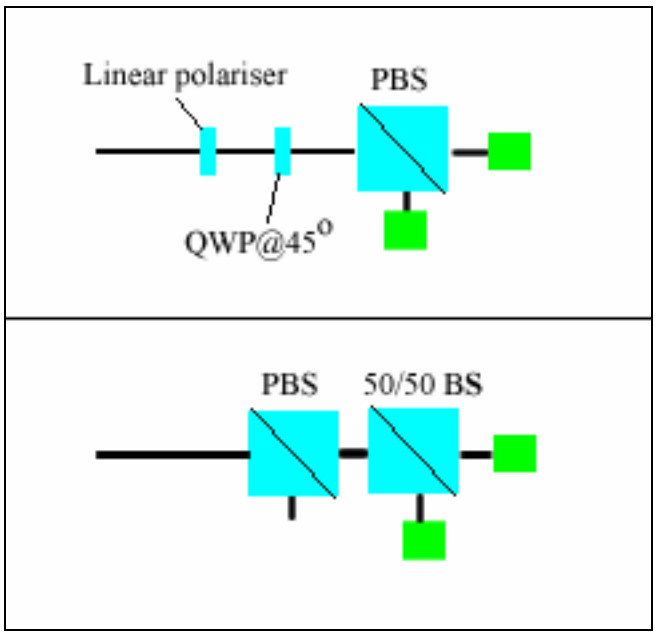

Figure 25 – Setup to distinguish HH and VV state

4.9 ELECTRONICS

Whenever the single photon detector saw a photon, it would generate a NIM pulse. A NIM pulse uses 0 V and -0.8 V for logic 0 and 1 respectively. Negative logic was used in this case to avoid the slow rise-time associated with positive logic. A NIM fanout was then used to split the signal from the detector into two. A normal T-junction could not be used in this case as the difference in impedance introduced by the parallel connection would cause the signal to be reflected at the connector and thus distorting the signal. The pulses from the four detectors were then passed through two manual delay cards where the signals could be delayed to compensate for any time difference between the propagation in the two channels. The signal then passes through a 16-fold coincidence card to search for any coincidence. By adjusting the pulse width at the manual delay, the coincidence window can be changed. The pulse

width was set to 4ns. Thus any pulses arriving within 8ns of each other were considered a coincidence. The signals from the coincidence card and the NIM fanout were then converted to TTL signal to be read by the computer through a digital counter card. The setup and a schematic of it are shown in Figure 26 and 27 respectively.

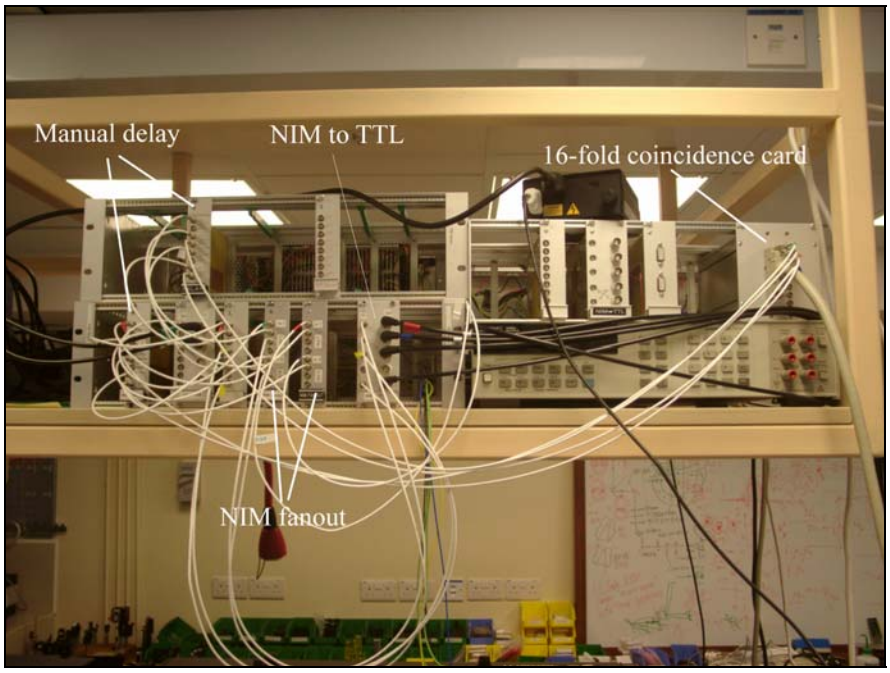

Figure 26 – Electronics of experimental setup

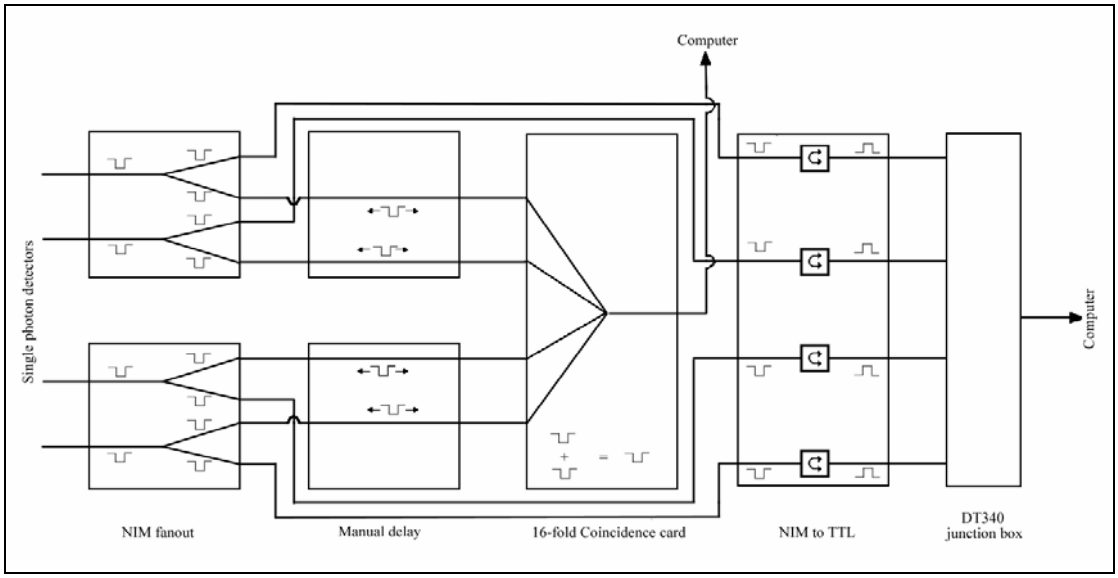

Figure 27 – Schematic of electronic setup

It was important that the signals from the 4 detectors took the same amount of time to reach the coincidence stage. To ensure that the correct delay was applied to all four channels, pulse from one was taken as the reference and the delay was then adjusted until the pulses from the other detector coincide with it.

4.10 NEUTRALISING THE FIBER

After the polarised light from the down-conversion process was collected by the collection optics, it was channelled through single-mode optical fibres to the analysers. It is important that the polarisation measured at the analyser was same as that incidence at the collection optics. If that were not the case, the correlation measured would not be as pronounce, thus degrading the quality of the entanglement detected. Thus there was a need for these fibers to be neutral; light exiting the fiber must have the same polarisation as that entering it. The fibers were neutralised by the

use of polarisation controllers, shown in Figure 28. In a polarisation controller, the fiber was looped into the three independent spools.

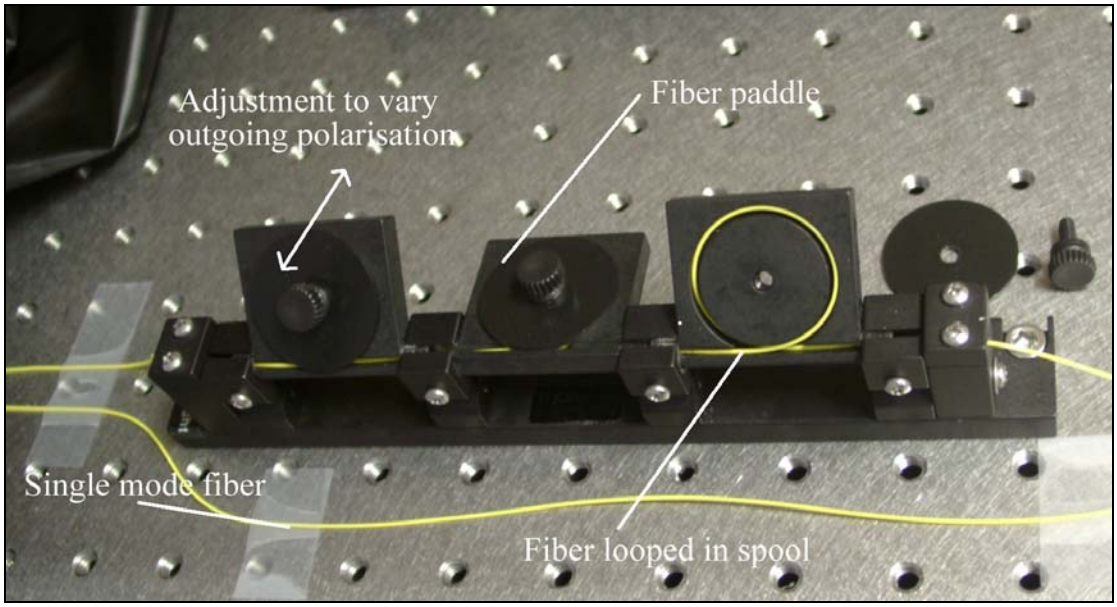

Figure 28 – Fiber polarisation controllers

The loops stressed the fiber thus inducing birefringence to produce the equivalent of three wave plates or retarders which were used to change the polarisation in the fiber. The amount of birefringence induced in the fiber was dependent on the fiber cladding and spool diameter, the number of fiber loops per spool and the wavelength of the light passing through it [22]. The desired output polarisation was then produced by turning the three paddles. To ensure that enough retardation was introduced between the polarisations, the fiber was looped 1, 2 and 1 times in the three spools respectively.

To neutralise the fiber, the setup shown in Figure 29 was used. Before the start of the procedure, the collection optics was adjusted to maximise the 780nm singles detected.

A polariser and a HWP, with both of their optical axis set to horizontal, were placed in front of the collection optics. A second half-wave plate also with its' optical axis set to horizontal was placed after the fibre. Both HWP were mounted on motorised rotation stages so that their orientation could be controlled accurately via computer. The polariser and HWP were specifically designed to work for small range of wavelength, around 800nm in this case. Thus for the unconverted 390nm light, the action of the polariser and HWP was not very pronounced. To ensure better suppression of the counts at the detector when the measurement basis was orthogonal to the polarisation of the incoming light, a 780nm interference filter (780BP5) was required after the second HWP. For this neutralisation procedure, the PBSs were left in the analysers.

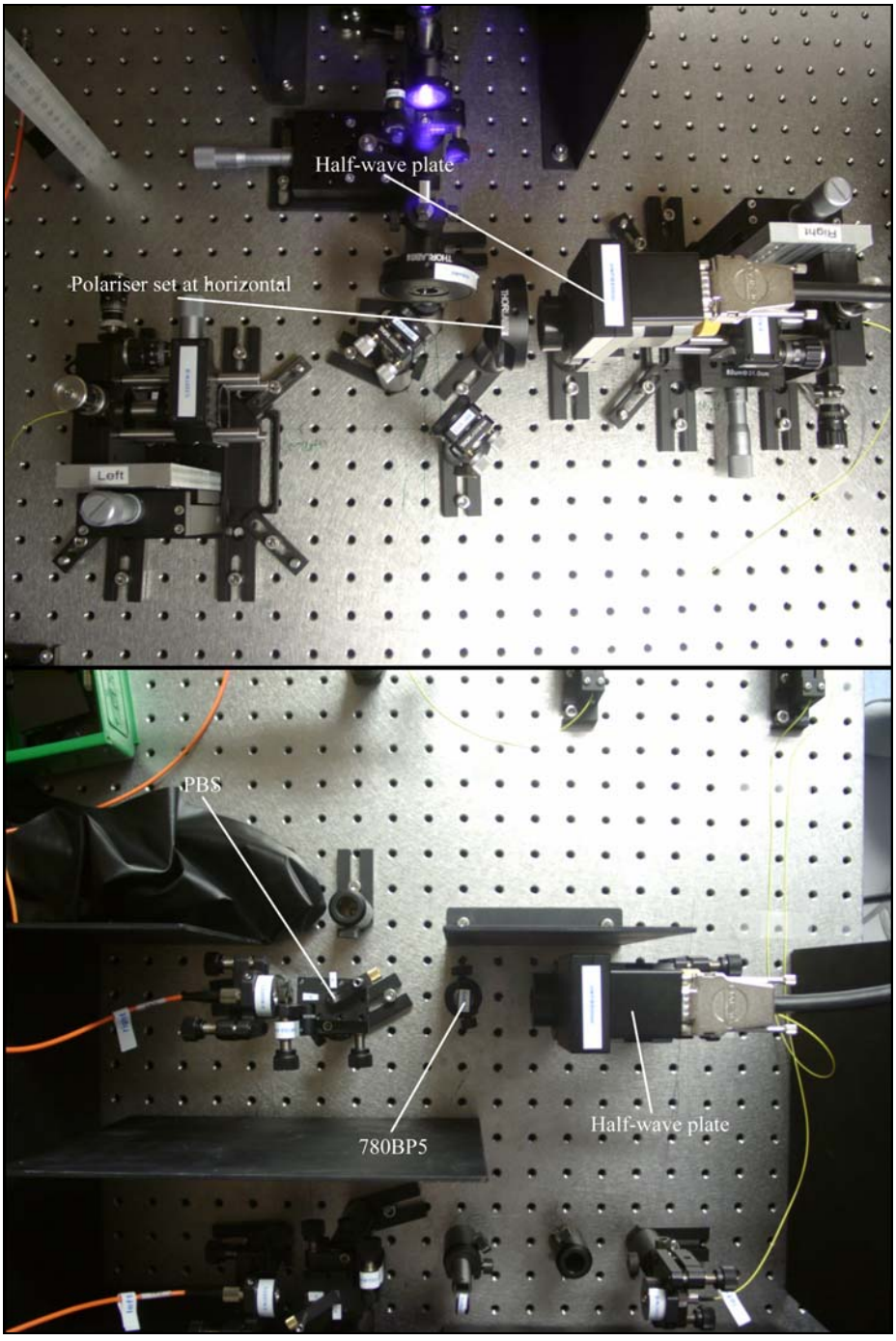

Figure 29 – Setup for neutralising fibre

The first step was to neutralise the fibre for the horizontal and vertical polarisations. One of the HWPs was rotated by 45^{o} thus turning the incoming light or measurement basis to vertical. With the measurement basis and the polarisation of the incoming

light orthogonal to each other, the fibre paddles were adjusted until the lowest counts was obtained. Alternatively, by not rotating the HWPs, the measurement basis and the polarisation of the incoming light were both horizontal and thus the counts needs to be maximised instead.

After the first step was completed, the fibre was neutralised for the horizontal and vertical polarisation with the exception of additional phases. For example

$$|H\rangle \rightarrow e^{i\theta}|H\rangle$$
$$|V\rangle \rightarrow e^{i\phi}|V\rangle$$

When a 45^{o} linearly polarised light was send in the collection optics, the fiber would induce a relative phase between the vertical and horizontal polarisation. For example, ignoring the global phase,

$$|H\rangle + |V\rangle \rightarrow |H\rangle + e^{i\delta}|V\rangle$$

Thus to eliminate this relative phase, the second step involved neutralising the fibre for the +45^{o} and -45^{o} basis. The HWPs were rotated to until the polarisation of the incoming light and the measurement at -45^{o} and +45^{o} respectively. The counts were then minimised by adjusting the fibre paddle. Similarly both half-wave plate could be rotated to the 45^{o} basis and the counts maximised instead. These two steps were repeated until the counts were minimum when the measurement basis and polarisation of the incoming were orthogonal and maximum when they were parallel.

4.11 LOCATING THE SPOT FOR THE DEGENERATE CASE

The next step in the assembly process was to ensure that the collection optics was collecting the down converted 780nm light from the intersection of the two emission cones. At this stage, the singles at 780nm should be fairly maxmised prior to neutralising the fibers. The next step was to maximise the coincidence. A useful guide was to look at the spectrum of each of the arms without the 780nm interference filter. From the spectrum three possible cases could be distinguished. The first case was when the spectrum exhibit two peaks one of them being at 780nm. This meant the collection optics was collecting light near the intersection of the emission cones. One of the peaks corresponded to the e-polarised light, the other to the o-polarised light. If one of the peaks was at 780nm, this meant that the collection optics was looking at the intersection of the emission cones of the 780nm light with the emission cone of some other wavelength. The second case was when one peak at 780nm was visible. Depending on the maximum counts, this could mean one of two things. The first was that the collection optics was looking at one of the 780nm emission cones in a region not near to the intersection. Thus the maximum count should be about half that detected at the intersection. The second case was the collection was looking at the correct spot at the intersection. The counts would be twice that of the case when the collection optics was not looking at the intersection. The situation could be verified by slight adjustment off the maximum. One should observe that the maximum count should decrease by half. The various situations are illustrated in Figure 30. After that is achieved, fine adjustments were then made to maximise the coincidence. The spectrum taken at each arm is shown in Figure 31.

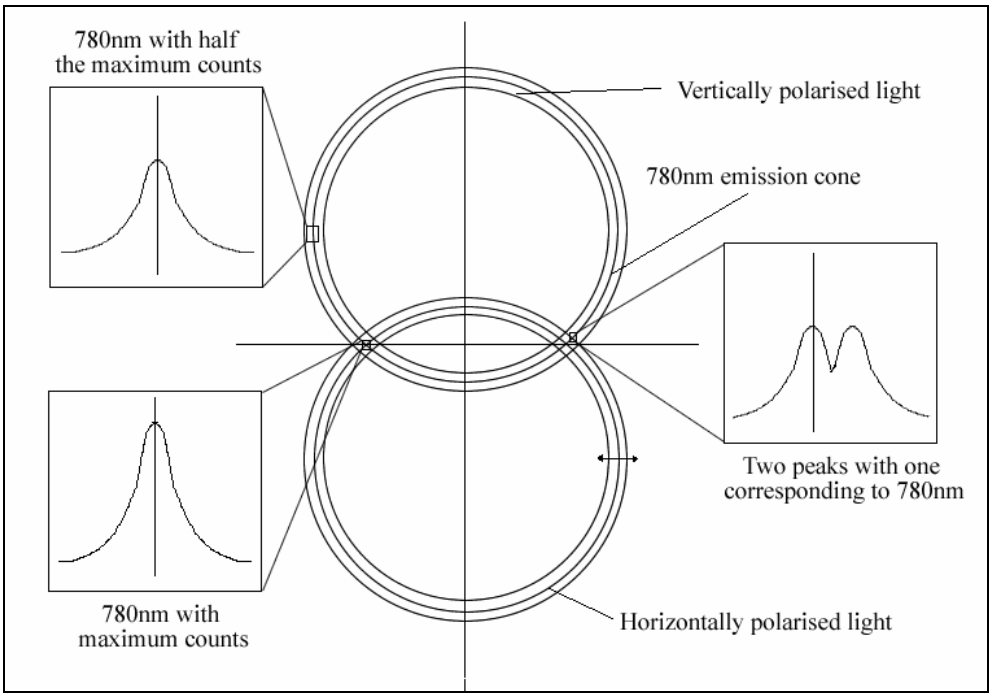

Figure 30 – Situation corresponding to different spectrum

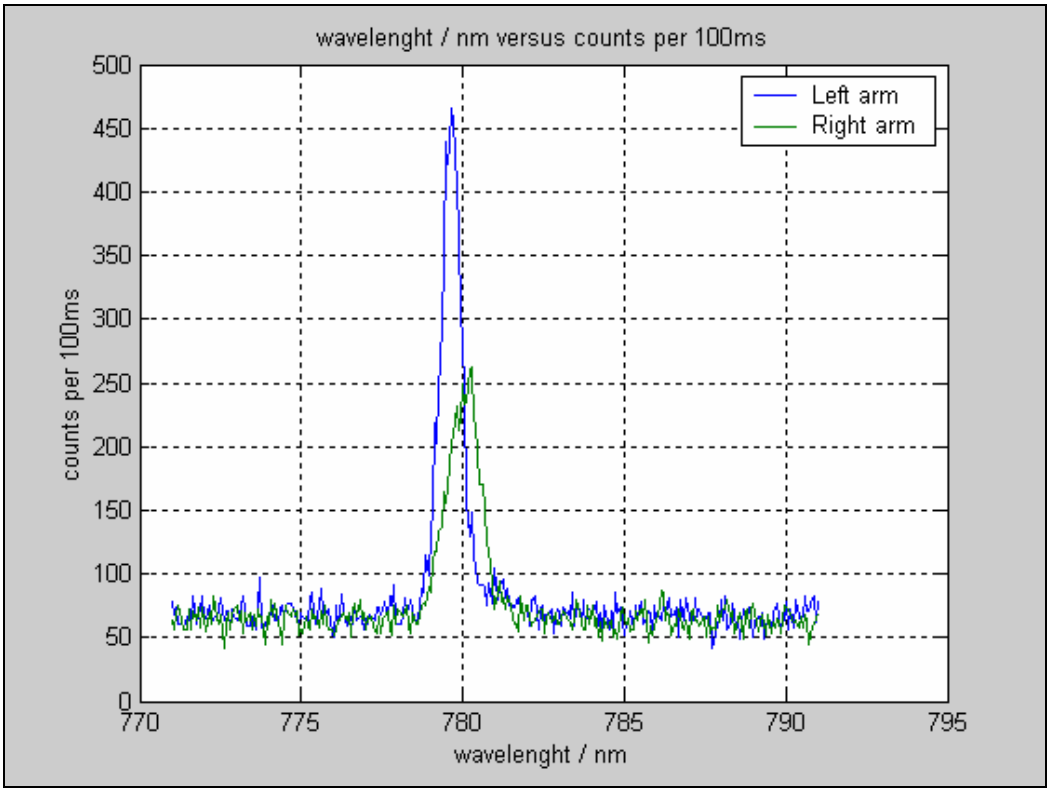

Figure 31 – Spectrum of light collected at each arm

From Figure 31, it can be seen that the spectrums contain only one peak. The low number of counts was attributed to the inefficient coupling in the analyser rather than the collection optics being pointed at the wrong spot on the crystal. Thus it was concluded that the collection optics was collecting light from the correct the region where the two cones intersects. To fine tune the alignment, the counts from each of the output port of each PBS could be monitored. Only when one was pointing at the intersection would the counts from the two ports be balanced. Slight misalignment from the intersection will show up as an unbalanced number of counts between H and V photons. After the initial alignment, the setup could then be maximised for coincidences.

4.12 ALIGNING THE COMPENSATOR CRYSTALS

BBO crystals are birefringent, having different refractive index for different polarisations. The refractive index for o-polarised ray is greater than that for e-polarised ray. That translates to a higher propagation velocity for the e-polarised ray in the crystal resulting in the e-polarised photon from a down-converted pairs to exit the crystal earlier than the o-polarised photon and thus arriving first at the detector. The difference in arrival time is dependent on where in the crystal the down conversion occurred. If the down-conversion occurs at the incident face of the crystal the difference in arrival time will be maximum as the o-polarised photon is delayed throughout the path through the crystal. On the other hand, if the down-conversion occurs on the face away from the pump source, there is no difference in arrival time as the path of the photon pairs does not go through the crystal. This difference in arrival time allows the distinction between the o and e-polarised photons to be made,

thus degrading the quality of entanglement. Only the photon pairs created at the face away from the source are truly entangled as there is no additional timing information that can be use to distinguish between the o and e-polarised photons. This phenomenon is termed temporal walkoff.

To correct for this temporal walkoff, BBO crystals of half the thickness of the down conversion crystal were placed just before each of the collection optics. The optical axis of the compensator crystals were placed perpendicular to that of the down conversion crystal. Thus relative to the compensator crystals, the o and e-polarised photon would appear to be e and o polarised respectively. For photon pairs that were created on the incident face of the crystal, the e polarised would reach the compensator crystal before the o-polarised photon. The o-polarised photon would now travel faster than the e-polarised photon in the rotated compensator crystal. As the thickness of the compensator crystals was half the down conversion crystals, the time difference in arrival time was reduced by half. For photon pairs that were created on the face away from the pump beam, both e and o-polarised photon would arrive at the same time at the compensator crystals. After passing through the compensator crystals, the o-polarised photon would exit before the e-polarised photon. Thus for any position at which down conversion occurs, there would be another position where order of arrival was reversed after passing through the compensator crystals. These two cases were diametrically opposite and cannot be distinguished. Thus the quality of entanglement was maintained. This is illustrated in Figure 32.

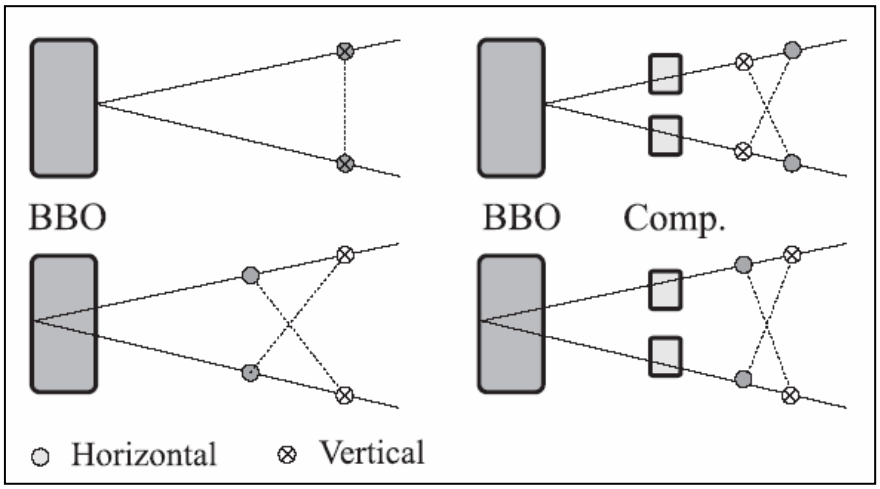

Figure 32 – How compensator crystal correct for temporal walkoff

While the first scheme addresses the problem of temporal walkoff, it inevitably introduces another problem. As the BBO crystals are birefringent, the o-polarised ray will travel straight through the crystal while the e-polarised will be deviated. This is termed spatial walkoff. The same principle is used to identify the direction of the optical axis of the BBO crystal. Thus if the first scheme is used, a horizontal walkoff will be introduced as the e and o-polarised ray passes through the compensator crystals. A better way will be to rotate the polarisation state of the photon by means of a half-wave plate set at an angle of 45^{o} to horizontal just after the down conversion crystal. The o-polarised ray coming out from the down-conversion crystal will be spread out. The half-wave plates then interchange the polarisation state of the two rays. After the compensator crystal, the now spread-out e-polarised ray will be shifted such that their centres will coincide. The situation is illustrated in Figure 33. The compensation setup is shown in Figure 34.

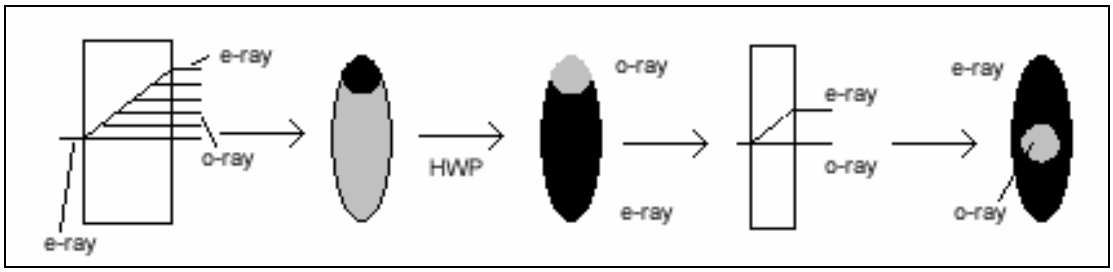

Figure 33 – Compensating for spatial walkoff

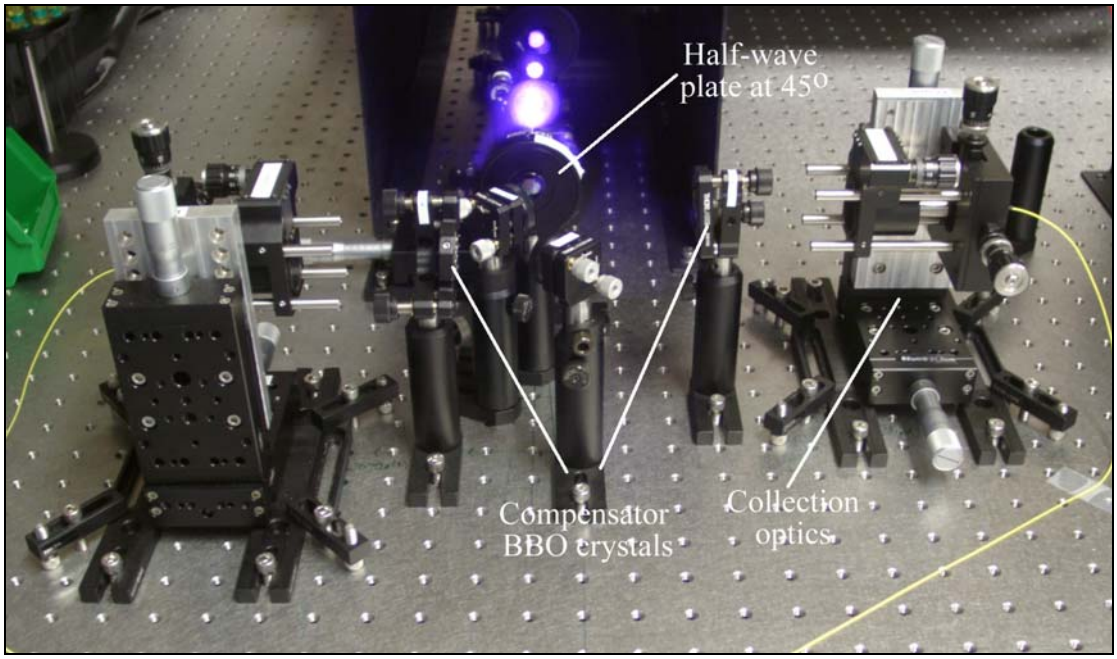

Figure 34 – Compensator BBO crystals placed before the collection optics

As the path of the e-polarised and o-polarised light through the compensator was different, a phase shift was induced between them. This phase shift corresponds to the angle φ in the state obtained from the down-conversion mentioned in chapter 3. By tilting the compensator crystals, this phase shift could be varied allowing different state to be produced. To align the compensator, the analysers were set to measure $+45^{o}$ and -45^{o} basis. The compensator was then tilted to minimise the coincidence. The situation was similar to that of the neutralisation of the fibers.

Chapter 5
EXPERIMENTAL PROCEDURES AND RESULTS

Once the number of coincidences had been maximised to approximately 10% of the singles, various measurement could then be done to ascertain the quality of entanglement that was obtained from the source. This chapter highlights some of these measurements conducted and the results obtained

5.1 2-PHOTON MEASUREMENTS

This first series of measurements were to determine the quality of entanglement of the 2-photon states. This was achieved by measuring the visibility in HV basis. If the visibility is less than

$$\frac{2}{S_{QM}} = \frac{2}{2\sqrt{2}} = 70.7\%$$

Bell's inequality would not be violated

5.1.1 VISIBILITY MEASUREMENT IN HV BASIS

In this visibility measurement for the 2-photon case, the HWP in one arm was kept fixed at horizontal, H, while the other was rotated from 0^o to 360^o in step of 1^o. Only counts from the straight-through port of the PBS in the analysers were taken. At every

angle, the total numbers of 2-fold coincidences in 1s were recorded. The data points were then fitted to the equation

$$y = A\sin(Bx + C) + D$$

in order to find the maximum and minimum rate of coincidence. The visibility was then calculated by the following

$$V = \frac{\mathrm{I}_{max} - I_{\min}}{\mathrm{I}_{max} + I_{\min}}$$

where I_{max} and I_{min} were then maximum and minimum coincidence rate and they correspond to the case when the sin function is +1 and -1 respectively. A plot of the data and the fit is shown in Figure 1.

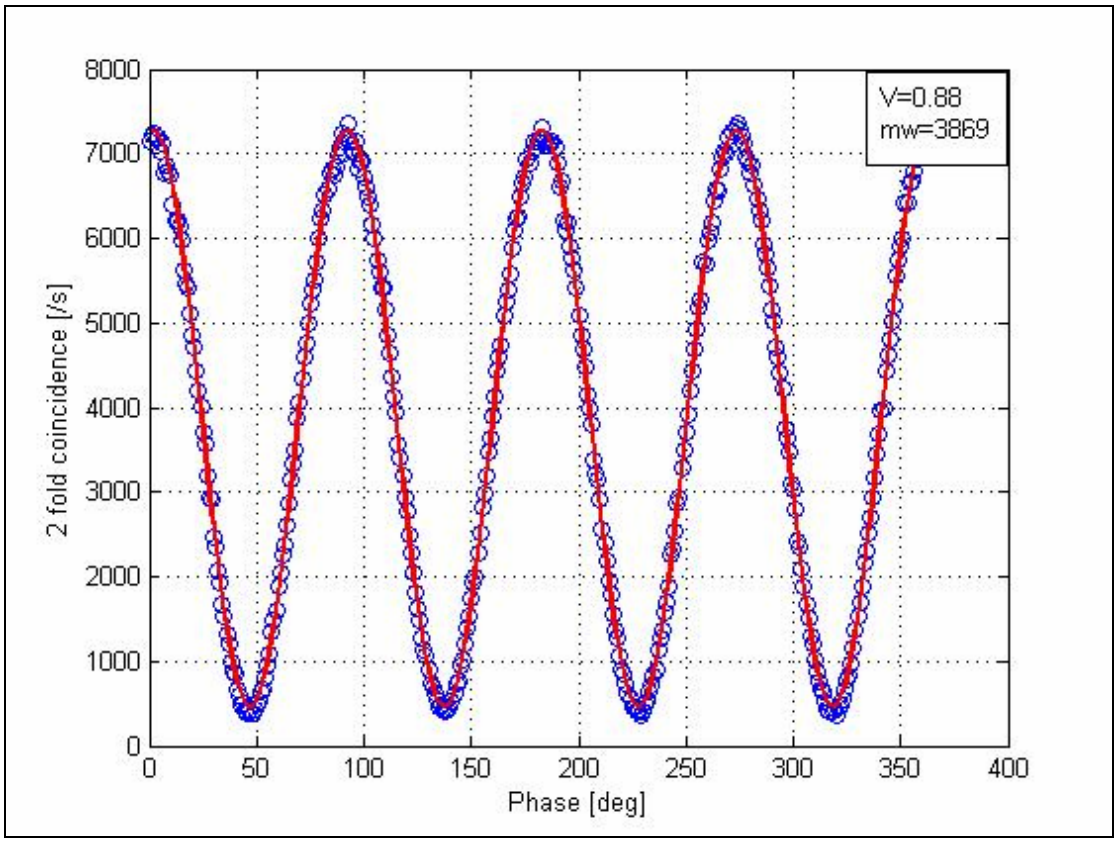

Figure 1 – A plot of data points and fit for the HV visibility

After fitting, the visibility was obtained to be 88%. Thus the setup can be used to violate the spin $-\frac{1}{2}$ Bell's inequality. From Figure 1 it can also be seen that the mean number of coincidences per second was about 4000 with a noise of about 400 coincidences per second. The plot also shows four cycles. This was to be expected as the HWP was rotated over 360^{o}, the measurement basis was rotated through 720^{o}. Within this 720^{o}, the measurement bases were parallel and perpendicular 4 times, thus producing cycles of coincidence counts seen in the plot The coincidences was

maximum when the measurement basis were at H and V respectively while it was minimum when they were at the same basis.

5.1.2 VIOLATION OF SPIN-1/2 BELL'S INEQUALITY

The procedure to violate the spin-$\frac{1}{2}$ Bell's inequality was a straight forward analogy of the actual Bell's inequality. For each of the correlation function corresponding to one of the four sets of possible analyser settings, there are 4 probability terms. Therefore 16 measurements of coincidences per second were needed. The 4 analyser settings that were used were the ones corresponding to the measurement basis shown in chapter 2 at which the quantum mechanics predicts maximum violation. The four analyser settings were 0^o, 11.25^o, 22.5^o and 33.75^o, half of that of the quantum mechanical prediction. This was because one set of angles refers to the rotation of the measurement basis while the other is the physical rotation of the HWP. The rotation of the HWP was always half that of the rotation of the physical basis.

From the individual coincidence readings, the correlation function for a specific set of analyser setting was the calculated using the following.

$$E(\alpha,\beta)^{QM} = \frac{N(+,+) - N(+,-) - N(-,+) + N(-,-)}{N(+,+) + N(+,-) + N(-,+) + N(-,-)}$$

The values of the 4 correlation functions were obtained to be

$$E(\alpha,\beta) = -0.5326339$$
$$E(\alpha,\beta') = -0.6988615$$
$$E(\alpha',\beta) = -0.61486346$$
$$E(\alpha',\beta') = 0.608905079$$

Therefore from value of the 4 correlation function the value of S was determined to be 2.446 ± 0.01014, violating the Bell's inequality by up to 43.98 standard deviations. The data is tabulated in the Appendix

5.2 4-PHOTON MEASUREMENTS

This second series of measurements were to determine the quality of entanglement for the 4-photon state. This was achieved by measuring the visibility in HV and ± 45^o basis. If the visibility is less than

$$\frac{2}{S_{QM}} = \frac{2}{2.55228} = 78.4\%$$

Bell's inequality will not be violated

5.2.1 VISIBILITY MEASUREMENT IN HV AND ± 45^O BASIS

The procedure for the visibility measurement of the 4-photon case in the HV and ±45^o basis was similar to that of the 2-photon case. A counting time of about 100s was used due to the low rate of 4-fold coincidences. For the HV basis, one of the HWP was fixed at the horizontal position while the other was rotated. For the ±45^o, one of the HWP was fixed at the +22.5^o while the other was rotated. In both cases, all four ports

were monitored to record the number of 4-fold coincidences. Plots of the data and the fit for the HV and ±45^{o} visibility measurements are shown in Figure 2 and 3 respectively.

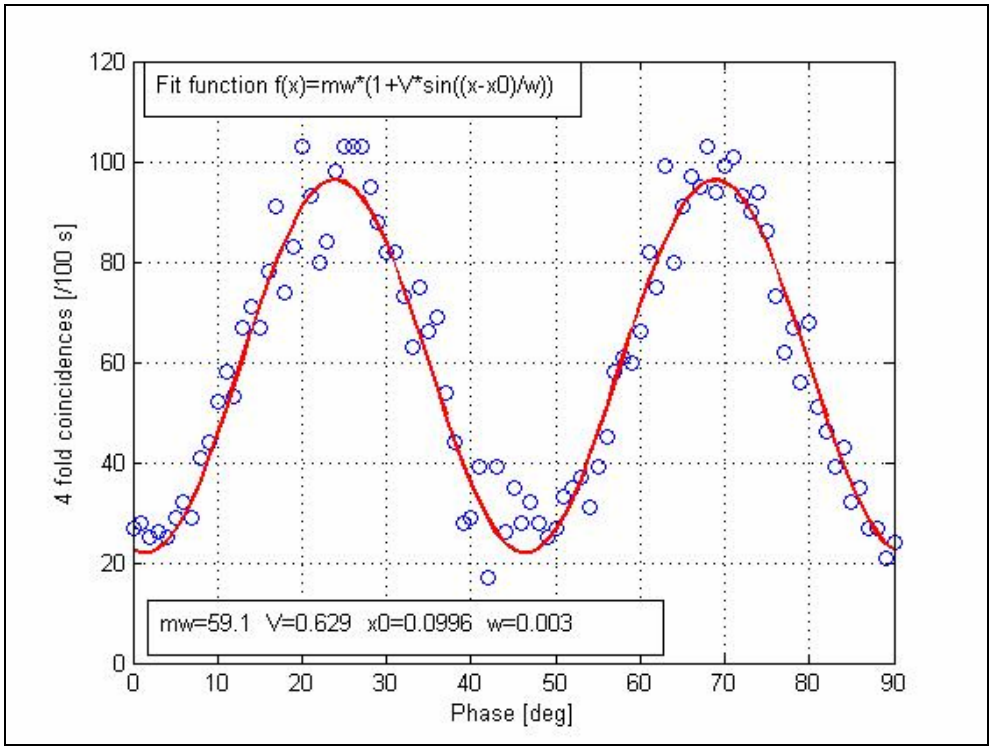

Figure 2 – A plot of data points and fit for the ±45^{o} visibility

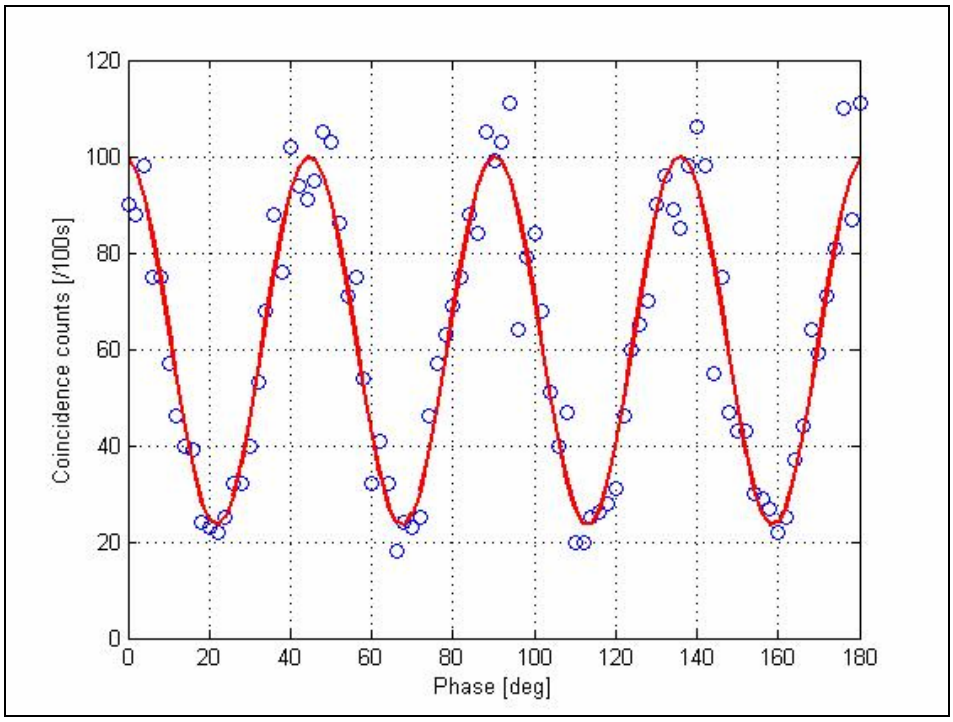

Figure 3 – A plot of data points and fit for the HV visibility

The two plots were 22.5^{o}out of phase. This was expected as it correspond a 45^{o} phase difference between the measurement bases. When both set of data were fitted to the sinusoidal equation, the visibilities were obtained to be about 63%. Therefore the setup was not able to be used to violate the spin-1 Bell's inequality. This was probably due to the fact that the alignment of the two collection optics still needs to be additional fine tuning.

CONCLUSIONS

While the spin-1 Bell's inequality was not successfully violated at the time of writing of this report, visibility measurements suggest that it is just a matter of further fine tuning to get the necessary visibility. The experimental objective of setting up a 4-photon source had been achieved. With this setup we have managed to show that even with a simple 1-pass scheme it was still possible to generate 4-photon states. The unarguably the most important point being the things learnt and the experience gained in the course of the experiment. A great deal was learnt about the steps that gone into setting up a 2 and 4-photon source, covering everything from the alignment to the detection electronics. The next step would be to further fine tune the setup to attain a higher visibility that is able violate the spin-1 Bell inequality. Once that is done, the door is open to many interesting experiment with using 4-photon states. First, we can characterise the noise to better understand its' source and how it will affect the degree of entanglement observed. Various experiments like the proposed 'Guess my number' protocol which uses a 4-photon GHZ state can also be carried out. With the rarity of 4-photon coincidence events, it is also worthwhile to look into the various new detection schemes which can be then be tested with this 4-photon source.

REFERENCES

[1] Aspect A., Dalibard, J. and Roger, G., "*Experimental test of Bell"s inequalities using time-varying analysers*", Phys. Rev. Lett., 49, 25 (1982).

[2] Aspect A., Grangier, P. and Roger, G., "*Experimental tests of realistic local theories via Bell's theorem*, Phys. Rev. Lett., 47, 7 (1981).

[3] Aspect A., Grangier, P. and Roger, G., "*Experimental realisation of Einstein-Podosky-Rosen-Bohm gedankenexperiment: A new violation of Bell"s inequalities*", Phys. Rev. Lett., 49, 2 (1982).

[4] Ballentine, L.E., "*Quantum mechanics: A modern development*", World Scientific Publishing Company (1988).

[5] '*BBO Properties - United Crystals Company*', http://www.unitedcrystals.com/BBOProp.html

[6] Bell, J.S., "*Speakable and Unspeakable in Quantum Mechanics*", Cambridge University Press (1987).

[7] Clauser, J.F., Horne, M.A., "*Experimental consequences of objective local theories"*, Phys. Rev. D, 10, 526-35 (1974).

[8] Clauser, J.F., Horne, M.A., Shimony, A. and Holt, R.A., "*Proposed experiment to test local hidden-variable theories*", Phys. Rev. Lett., 23, 880-884 (1969).

[9] Coherent, "*Operator"s Manual MIRA-900F Modelocked Ti:Sapphire Laser*".

[10] Coherent, "*Operator"s Manual Vertic*^{TM} *V-8/V-10 Diode-pumped Laser*".

[11] Einstein, A., Podolsky, B. and Rosen, R., "*Can quantum mechanical reality considered to be complete?*", Phys. Rev., 47, 777 (1935).

[12] Hecht, E., "*Optics*", Addison Welsey (2002).

[13] Howell, J.C., Lamas-Linares, A., Bouwmeester, D., "*Experimental violation of a spin-1 Bell inequality using maximally entangled four-photon states*", Phys. Rev. Lett., 88, 030401 (2002).

[14] Kurtsiefer, C., Oberparleiter, M. and Weinfurter, H., "*High-efficiency entangled photon pair collection in type-II parametric fluorescence*", Phys. Rev. Lett., A.64 (2001).

[15] Kwiat, P.G., Mattle, K., Weinfurter, H. and Zeiling, A., "*New high-intensity source of polarisation-entangled photon pairs*", Phys. Rev. Lett., 75, 24 (1995).

[16] Pedrottti, F.L., Pedrotti, L.S., "*Introduction to Optics*", Prentice-Hall International, Inc. (1996).

[17] '*Reflection, Transmission and Phase Shift*', http://www.cvilaser.com/static/FRE

[18] Thompson, C.H., "*Timing, accidentals and other artifacts in EPR Experiments*", arXiv:quant-ph/9711044 v2 (1997).

[19] Thorlabs: "*BB1-E01 Specifications*".

[20] Thorlabs: "*BB1-E03 Specifications*".

[21] Thorlabs: "*C220TM-B Specifications*".

[22] Thorlabs: "*Fiber Polarisation Controller – FPC560*" (1998).

[23] Sutherland, R.L., "*Handbook of nonlinear optics*", Marcel Dekker, Inc. (1996).

[24] Wherrett, H., "*Nonlinear optics*", Academic Press (1977).

APPENDIX

PROFILE OF GAUSSIAN BEAMS

One of the most fundamental modes of light is the Gaussian beam. The laser used in this experiment is producing a circular beam with TEM_{00} mode or the Gaussian mode. The mathematical description of the Gaussian mode [16] is

$$w(z)^2 = w_0^2\left[1+\left(\frac{\lambda z}{\pi w_0^2}\right)^2\right]$$

where w is the spot size, w_0 the waist of the beam, z the distance from w_0 and the λ wavelength of the light. The situation is shown in Figure 1.

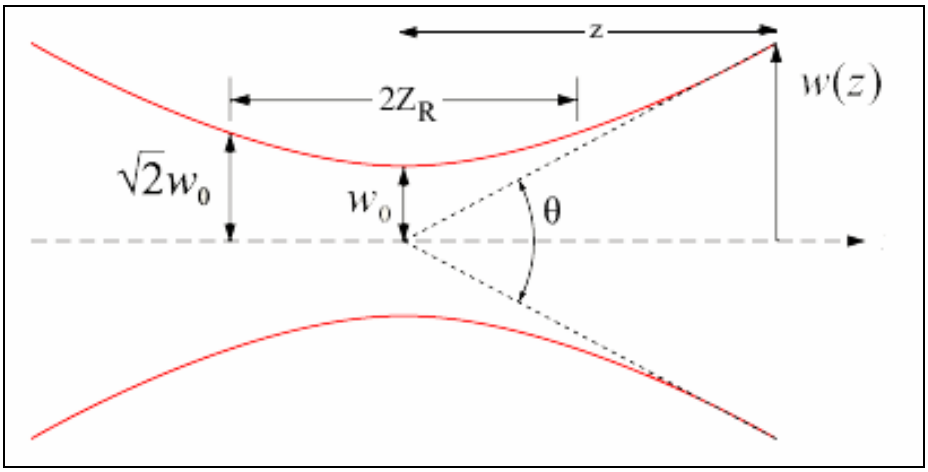

Figure 1 – A Gaussian beam

The transverse intensity profile of a Gaussian beam is described by the following

$$I(r) = I_0 \exp\left(\frac{-2r^2}{w^2}\right)$$

where I_0 is the maximum intensity of the beam and r the distance from the centre of the beam. Integrating the above equation over the diameter of the beam, the following error function is obtained

$$erf(x) = I_0 \int_{-w}^{x} \exp\left[\frac{-2r^2}{w^2}\right] dr$$

The procedure for waist measurement is described in chapter 4. The data obtained is fitted to the above error function.

Another associated quantity is the Rayleigh length. It is defined as the distance from the beam waist w_0 to the transverse plane where w(z) has the value $\sqrt{2}w_0$. By setting $w(z) = \sqrt{2}w_0$ the Rayleigh length Z_R is obtained to be

$$Z_R = \frac{\pi\omega_0^2}{\lambda}$$

The collimated region extends over two Rayleigh lengths, one on either side of the beam waist. Thus in the experiment, to ensure that the beam is transverse at the BBO crystals, it is important that it be placed within the Rayleigh length of the beam waist. For a 780nm and 390nm beam with a waist of 80μm, the Rayleigh lengths are about

2.58cm and 5.15cm respectively. The divergence of the beam is described by the following

$$\theta = \frac{2\lambda}{\pi\omega_0}$$

Thus it can be seen the smaller the waist of a beam, the faster it diverges and the smaller the Rayleigh length.

WAVE PLATES

Wave plates or retarders do not remove any polarisation components like the linear polarisers. Instead, they introduce a phase shift between them. This is achieved by means of birefringent materials which have different refractive indices for different polarisations. Two commonly used wave plates are the half-wave plate (HWP) and the quarter-wave plate (QWP). The HWP introduces a phase shift of π while the QWP induces a phase shift of $\frac{\pi}{4}$. There are two axis associated with a wave plate, the fast and slow axis. The wave plate will not have any effect on light polarised in the direction parallel to the fast axis. The action of a HWP and QWP are shown in Figure 1. Since wave plates introduce a phase shift between the two orthogonal components, they are used to change the state of polarisation of light.

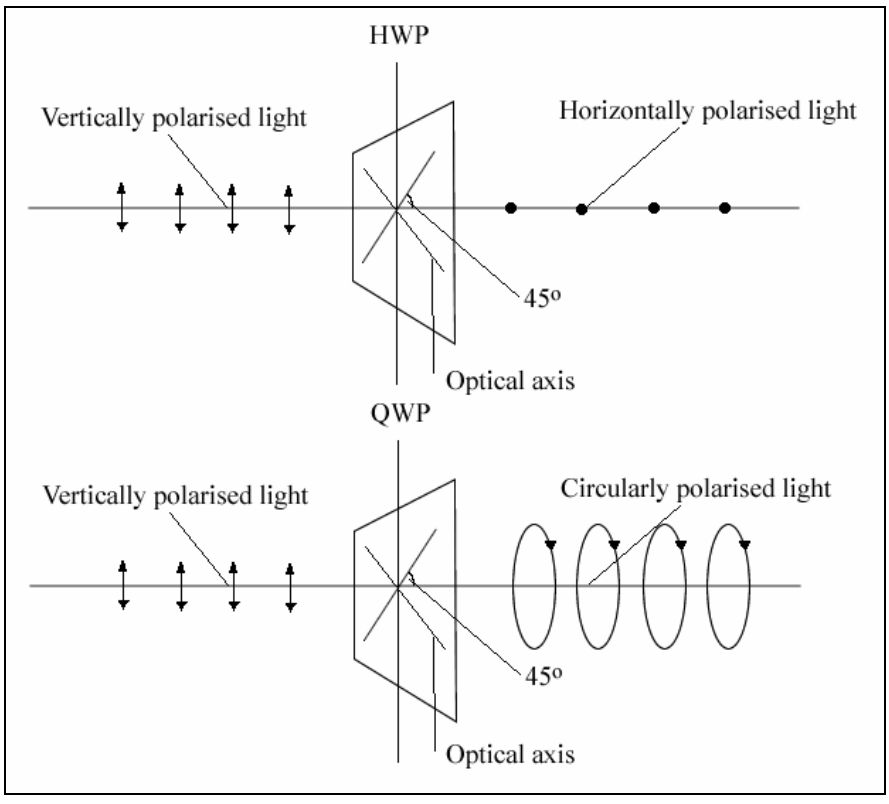

Figure 1- Action of a HWP and QWP

For an arbitrary angle, the matrix describing the action of a HWP is

$$e^{-i\frac{\pi}{2}}\begin{pmatrix}\cos 2\theta & \sin 2\theta \\ \sin 2\theta & -\cos 2\theta\end{pmatrix}$$

From the above matrix, it can be seen that the HWP always rotate the polarisation of the incident light through an angle twice that between the optical axis and the incident polarisation. For the QWP, the matrix is

$$\frac{1}{\sqrt{2}}\begin{pmatrix}\cos 2\theta + i & \sin 2\theta \\ \sin 2\theta & i - \cos 2\theta\end{pmatrix}$$

GLAN-THOMPSON POLARISERS

A Glan-Thompson polariser consists of two birefringent prisms cemented together. This is shown Figure 1. The different refractive index for the e and o-polarisation means that their path is different. The o-polarisation will arrive at the interface between the two prisms at greater than critical angle and is reflected at an acute angle from the path of the beam while the e-polarisation passes through the interface and the second prism with a small deviation.

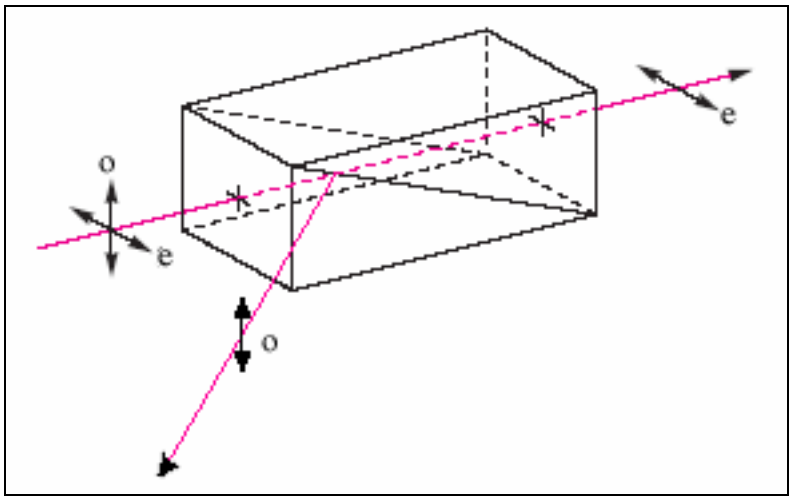

Figure 1 – Action of a Glan-Thompson polariser

DATA FOR VIOLATION OF SPIN-1/2 BELL'S INEQUALITY

	HH	HV	VH	VV
AB	2919	8761	9419	2765
A'B	2586	9646	9780	2047
AB'	1820	10028	10490	1817
A'B'	8948	2858	1973	10926